MODELING, SIMULATION, AND CONTROL OF AN AUTOMOTIVE EVAPORATOR

A Dissertation
Presented to
The Academic Faculty

By

Lachlan Page

In Partial Fulfillment
of the Requirements for the Degree
Master of Science in the
George W. Woodruff School of Mechanical Engineering

Georgia Institute of Technology

Dec 2020

MODELING, SIMULATION, AND CONTROL OF AN AUTOMOTIVE EVAPORATOR

Thesis committee:

Prof. Bert Bras, Advisor
School of Mechanical Engineering
Georgia Institute of Technology

Prof. Dr.-Ing. Dr. h.c. Oliver Sawodny
Institute for System Dynamics
University of Stuttgart

Prof. Marta Hatzell
School of Mechanical Engineering
Georgia Institute of Technology

Prof. Dr.-Ing. Cristina Tarín
Institute for System Dynamics
University of Stuttgart

Date approved: December 4, 2020

ACKNOWLEDGMENTS

I would like to thank Dr. Paul Neitzel, Dr. Andrei Fedorov, and Dr. Oliver Sawodny for giving me the opportunity to participate in this Joint Master's program. This has been the best experience I could have possibly hoped for, and I hope this program continues to provide opportunities to future students.

I would also like to thank my thesis advisor, Stefanie Göltz, for all the guidance she has given me throughout my time in Germany. She kept me on track and helped me get past numerous hurdles in this project, and I owe my success to her.

During my time at Georgia Tech, I had the privilege of working with Dr. David MacNair and with Dr. Bert Bras, who both helped me develop myself academically and professionally. I would also like to thank Dr. Bras, Dr. Marta Hatzell, Dr. Sawodny, and Dr. Cristina Tarín for serving on my reading committee.

Lastly, I would like to thank my friends and family who supported me throughout this program, especially Samuel Tovey and Peter Somers for helping me in adjusting to life in Germany. This was a stressful period, but you two made my time there a wonderful experience.

TABLE OF CONTENTS

LIST OF TABLES

LIST OF FIGURES

LIST OF ABBREVIATIONS

AC	Air Conditioning
EXV	Expansion Valve
FV	Finite Volume
MIMO	Multi-Input Multi-Output
MPC	Model Predictive Control
MPE	Mean Percent Error
MTE	Mean Temperature Error
ODE	Ordinary Differential Equation
OP	Operating Point
PDE	Partial Differential Equation
PID	Proportional-Integral-Derivative
SISO	Single-Input Single-Output
SMC	Sliding Mode Control

SUMMARY

As global climate change continues to affect everyday life, energy efficiency is becoming more crucial. Automotive emissions contribute a sizeable portion of man-made pollution, so a shift to "greener" automobiles has become paramount. Since automotive air conditioning systems are one of the biggest energy needs within a vehicle, increasing air conditioning efficiency can reduce the carbon footprint and increase the range of vehicles on the road today.

This paper works towards this goal by focusing on control of an automotive evaporator in tandem with an expansion valve and a compressor. The partial differential equations describing the evaporator thermal dynamics are developed using first principles and are then converted into ordinary differential equations using finite volume discretization. Parameter identification is performed by comparing simulations of the evaporator with physical measurements and minimizing the discrepancies. After the model is validated, a sliding mode controller is developed to regulate the outlet air temperature, and its performance is compared to that of a proportional integral derivative controller similar to what may be currently utilized in production vehicles. The results from simulation indicate that the sliding mode controller operates with better temperature tracking and uses less energy, and both controllers are ready for testing on a physical system.

CHAPTER 1
INTRODUCTION

Global warming has become a critical issue facing society, and governments have begun focusing on reducing their carbon footprints. This includes reducing pollution from the transport sector, which accounted for 14 % of all greenhouse gas emissions in 2010 [1]. To this end, automobile manufacturers are working to increase the efficiency of their vehicles through a variety of research projects.

Aside from the powertrain, the air conditioning (AC) uses the largest portion of the energy within a vehicle and can therefore negatively impact the driving range and efficiency ([2], [3]). Increasing the efficiency of an AC system is therefore an effective method to reduce a vehicle's carbon footprint. This work focuses on the development of a model-based nonlinear controller which will be compared to a common linear controller for a Daimler AC system evaporator. The goal of this work is to design a controller that can be adapted to a variety of evaporators which are subject to parameter uncertainties. Despite the uncertainties, the controller must be sufficiently robust to accurately track the desired output.

A general overview of the refrigerant circuit used in the EV and at the test bench is given, and the method used to filter the test bench data for system identification is presented. Afterwards, a continuous, nonlinear model for the evaporator is developed. The model consists of partial differential equations (PDEs) that are difficult to solve, so a finite volume approximation is used to allow efficient simulation. System identification is performed, and the parameters are validated through simulation and comparison with several data sets.

Once the parameters are determined to provide sufficient model accuracy, a proportional integral derivative (PID) controller and a sliding mode controller (SMC) are

developed. The stability of the SMC and the zero dynamics is proven through Lyapunov's theorem and linearization, respectively, and the controllers are then tested with a variety of disturbance values to ensure safe operation for the test bench. The tests are run for two different temperature profiles, and the mean air outlet temperature error and compressor speed are calculated and compared for both trials.

CHAPTER 2

VAPOR COMPRESSION CIRCUIT AND DATA PROCESSING OVERVIEW

This chapter introduces the vapor compression refrigerant circuit, which is the same circuit used in [4], that is analyzed for this work. A general overview of the circuit and a more detailed look into the evaporator are given, and the method used to filter the measurement data sets is discussed.

2.1 Vapor Compression Refrigerant Circuit

The general diagram of the refrigerant circuit, which utilizes refrigerant R1234yf, is obtained from Daimler and is shown in Figure 2.1a. The cycle operates between the points shown as follows:

1→2: Refrigerant passes through the expansion valve, resulting in a pressure drop to the cycle's low pressure. Specific enthalpy, however, is assumed to remain constant.

2→3: The evaporator heats up the refrigerant at constant pressure. Exiting refrigerant is typically superheated vapor.

3→4: In the low pressure side of the intermediate heat exchanger, the refrigerant is further heated up.

4→5: Refrigerant pressure is increased to the cycle's high pressure by the compressor.

5→6: The condensers cool the refrigerant down at constant pressure.

6→1: The refrigerant is further cooled down as it passes through the high pressure side of the intermediate heat exchanger and returns to the expansion valve as a subcooled liquid.

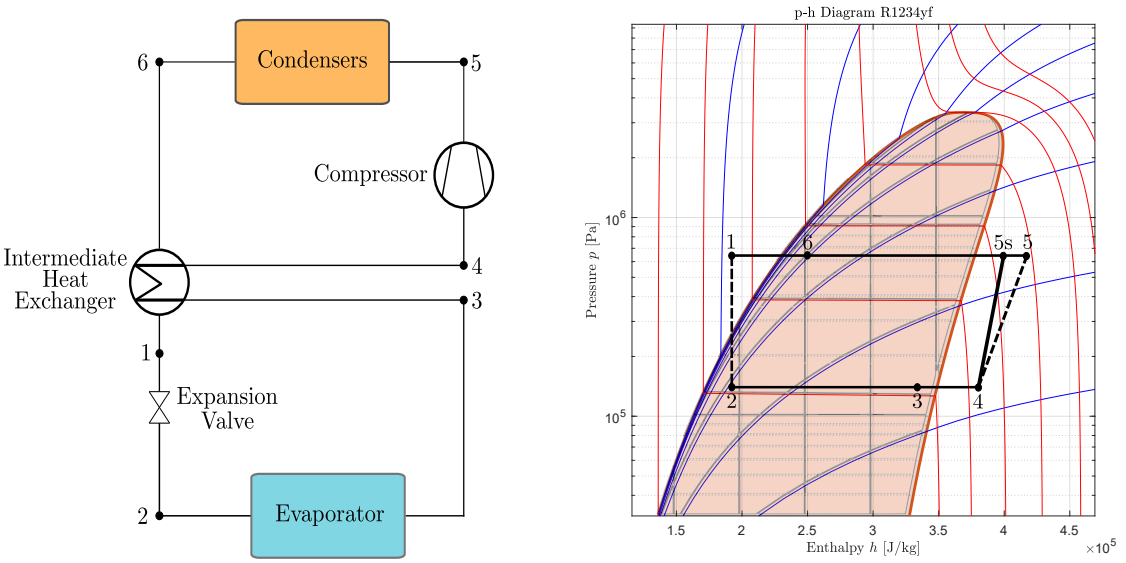

(a) Diagram of vapor compression circuit components.

(b) P-h Diagram of vapor compression circuit [5].

Figure 2.1: Vapor compression circuit overview.

Note that the points on the p-h diagram in Figure 2.1b serve only as an example and do not represent the exact operating points used in this work. The shaded area in the p-h diagram represents the two-phase region where the refrigerant consists of both liquid and vapor phases. The area to the left of this region corresponds to sub-cooled liquid, and the area to the right corresponds to superheated vapor. For additional reference, the red lines represent isotherms, and the blue lines represent constant density.

It is also worth noting that for an ideal compressor, the cycle will go from point 4 to point 5s rather than to point 5. In operation, however, the compressor does not operate in an ideal manner, and thus the entropy of the refrigerant increases depending upon the isentropic efficiency [5]. While the condensers influence the behavior of the evaporator and the expansion valve, it is assumed that they operate at constant pressure and provide sufficient cooling for the cycle. Therefore, for the sake of air conditioning, the focus of the controller design lies on the expansion valve, the

compressor, and the evaporator.

2.2 Evaporator

In order to cool the air, the system utilizes an aluminum plate evaporator, shown in Figure 2.2, in which the refrigerant makes multiple passes across the airflow. Due to the expansion valve, the refrigerant going into the evaporator is at low pressure and temperature, which indirectly cools down the air by cooling down the evaporator itself. The addition of fin-like structures between the refrigerant tubes increases the heat transfer surface area between the air and the evaporator, thus allowing for more efficient operation.

As shown in the p-h diagram in Figure 2.1b, the refrigerant entering the evaporator is typically a two-phase mixture. As the refrigerant passes through the evaporator, its enthalpy increases at constant temperature and pressure. In the event that the refrigerant exiting the evaporator is not superheated, it is assumed that the intermediate heat exchanger increases the enthalpy enough so that the refrigerant entering the compressor is a superheated vapor.

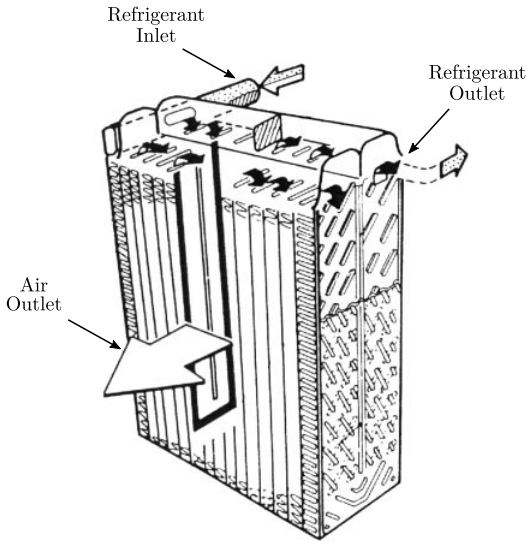

Figure 2.2: General plate evaporator illustration [6].

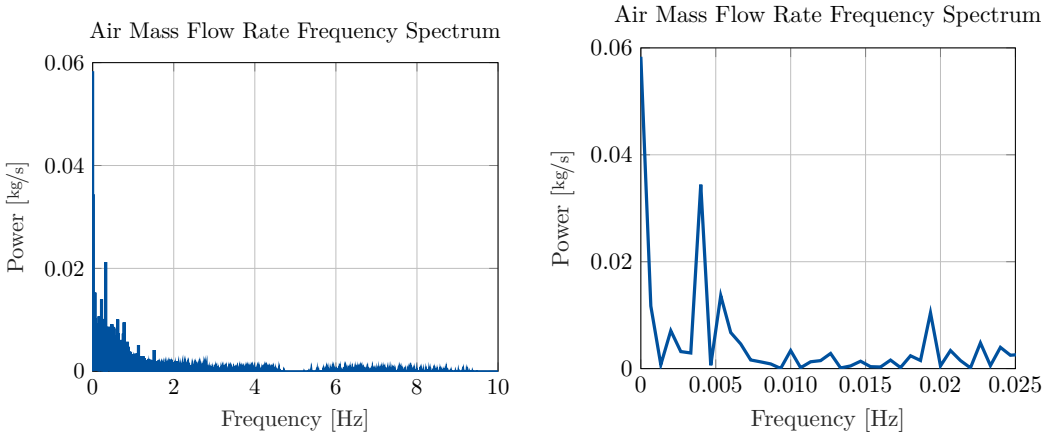

(a) Frequency spectrum of air inlet mass flow rate.

(b) Zoomed in view of the air mass flow rate frequency spectrum.

Figure 2.3: Air inlet mass flow rate frequency spectrums.

2.3 Data Processing and Calculation

The data recorded at the test bench, including the air velocity used to calculate the air mass flow rate, has significant noise distorting the signal. To mitigate this, the frequency spectrum of each signal is analyzed using the fast Fourier transform in Matlab. Once a suitable cutoff frequency is chosen, a Butterworth filter is designed and implemented it on each signal via the filtfilt() function in Matlab, which runs the filter forwards and then backwards to prevent the signals from shifting. The frequency spectrum of the air mass flow rate is shown in Figure 2.3a, and a more detailed view at lower frequencies is shown in Figure 2.3b. As in [4], the cutoff frequency ω_c is selected as 0.005 Hz, and an example unfiltered air mass flow rate signal is compared to its filtered signal in Figure 2.4.

In addition to noise issues, some values that are necessary for analysis, such as specific enthalpy, cannot be directly measured. This is solved by utilizing the state principle [5], which shows that for a pure substance, knowledge of two independent states is required to calculate the other states. Therefore, the refrigerant pressure and temperature, which are directly measured throughout the system, are used to

calculate the specific enthalpy via the CoolProp add-on in Matlab. Although point 2 of the cycle typically lies within the two-phase region, where the pressure and temperature are not independent, the assumption that the specific enthalpy does not change through the expansion valve allows for estimation of the this value. If point 3 lies within the two-phase region, it is assumed that the refrigerant is close enough to saturation to use the specific enthalpy of saturated vapor at the evaporator pressure. Additional assumptions regarding the evaporator are covered in Chapter 3.

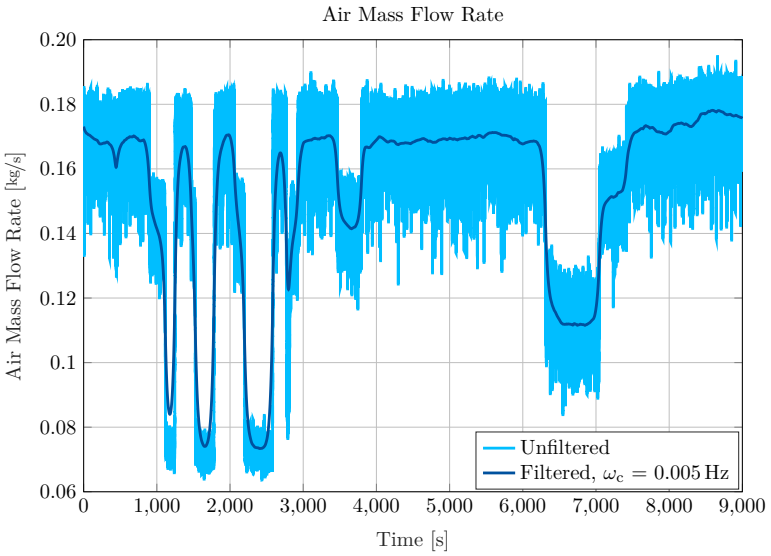

Figure 2.4: Comparison of unfiltered and filtered air mass flow rate signals.

CHAPTER 3

EVAPORATOR MODELING

The two most common methods for modeling and simulating heat exchangers are the finite volume (FV) and moving boundary methods [7]. While the moving boundary method provides approximately the same accuracy with reduced computation time, finite volume provides more robustness to various operating conditions [7], so this method is used in this work. This chapter begins with the derivation of the partial differential equations for the evaporator. The equations are then converted into ordinary differential equations (ODEs) via the FV method. These ODEs allow for efficient system simulation within Simulink, but certain parameters of the evaporator must first be identified. The parameters are identified by minimizing the weighted errors of the refrigerant pressure, refrigerant outlet specific enthalpy, and the air outlet temperature, and then the model is verified through simulation and comparison with several different data sets.

3.1 Evaporator Governing Equations

The evaporator used is a cross-flow heat exchanger similar to that used in [8]. As such, similar assumptions are used to simplify the model:

- The pressure drop and viscous effects throughout the evaporator are negligible.
- The refrigerant crosses the air stream only once.
- Heat transfer coefficients are the same for sub-cooled, saturated, and superheated phases.

- Only heat transfer between the refrigerant, the evaporator structure, and the air flowing through the evaporator is considered.
- The length of the refrigerant path through the evaporator will be normalized using a variable $z \in [0, 1]$.
- The air flow into the evaporator is uniform.
- The air is an ideal gas at constant atmospheric pressure.

3.1.1 Conservation of Mass - Refrigerant

The governing equations for the refrigerant and the evaporator structure (referred to from now on as the tube) will be derived by considering an infinitesimal control volume, as shown in Figure 3.1. The principle of conservation of mass for the refrigerant can be expressed as

$$\frac{dm}{dt} = \dot{m}(\tilde{z}, t) - \dot{m}(\tilde{z} + d\tilde{z}, t) = \frac{\partial}{\partial t}\rho(\tilde{z}, t)A_{\text{cs}}, \tag{3.1}$$

where the refrigerant mass flow rate $\dot{m}(z, t)$ and the refrigerant density $\rho(z, t)$ are one-dimensional variables [9], and A_{cs} represents the refrigerant cross sectional area, which is constant. Utilizing a first-order Taylor series approximation [10], Equa-

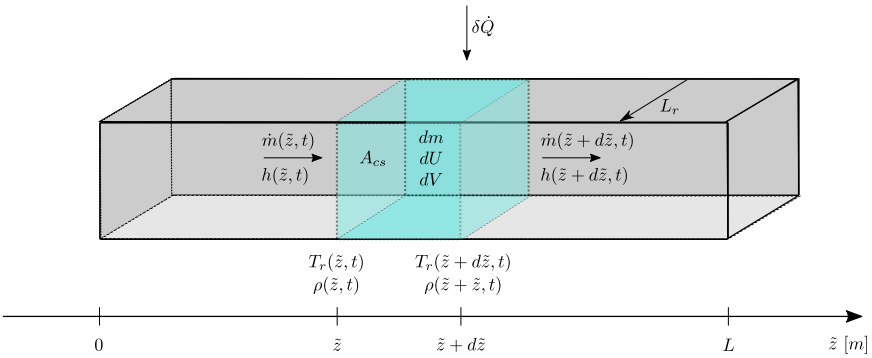

Figure 3.1: Infinitesimal refrigerant control volume [9].

tion 3.1 can be rewritten as

$$A_{\text{cs}}\frac{\partial}{\partial t}\rho(\tilde{z},t) \approx \dot{m}(\tilde{z},t) - (\dot{m}(\tilde{z},t) + \frac{\partial}{\partial \tilde{z}}\dot{m}(\tilde{z},t)), \tag{3.2}$$

and thus, after substituting $\tilde{z} = zL$, the conservation of mass can be shown by

$$V\frac{\partial}{\partial t}\rho(z,t) + \frac{\partial}{\partial z}\dot{m}(z,t) = 0, \tag{3.3}$$

where V is the refrigerant volume, and $z \in [0,1]$.

3.1.2 Conservation of Energy - Refrigerant

Referring again to the control volume shown in Figure 3.1, the first law of thermodynamics [5] is applied with the same method as [9] and [4] to obtain

$$\begin{aligned}\frac{dE}{dt} =& \dot{m}(\tilde{z},t)\left(h(\tilde{z},t) + \frac{v^2(\tilde{z},t)}{2} + gy(\tilde{z},t)\right) \\ &- \dot{m}(\tilde{z}+d\tilde{z},t)\left(h(\tilde{z}+d\tilde{z},t) + \frac{v^2(\tilde{z}+d\tilde{z},t)}{2} + gy(\tilde{z}+d\tilde{z},t)\right) \\ &+ d\dot{Q} + \dot{W},\end{aligned} \tag{3.4}$$

where E is the energy in the control volume, h is the refrigerant specific enthalpy, v is the refrigerant velocity, y is the height of the refrigerant, g is the gravity constant, $\dot{Q}$ is the heat transfer rate from the tube to the refrigerant, and $\dot{W}$ is the work done by the refrigerant. The kinetic and potential energies are considered to be negligible in this application, so E can be considered to be equivalent to the control volume internal energy U. Assuming the refrigerant work to be negligible as in [9] and [4], Equation 3.4 is reduced to

$$\frac{dU}{dt} = \dot{m}(\tilde{z},t)h(\tilde{z},t) - \dot{m}(\tilde{z}+d\tilde{z},t)h(\tilde{z}+d\tilde{z},t) + d\dot{Q}. \tag{3.5}$$

Noting that for constant pressure,

$$dU = dH - pdV = dzA_{\mathrm{cs}}\left(\rho(\tilde{z},t)h(\tilde{z},t) - p(t)\right), \tag{3.6}$$

and that from [10], the heat transfer rate can be expressed as

$$\dot{Q} = d\tilde{z}L_{\mathrm{r}}\alpha_{\mathrm{r}}\left(T_{\mathrm{t}}(\tilde{z},t) - T_{\mathrm{r}}(\tilde{z},t)\right), \tag{3.7}$$

where $d\tilde{z}L_{\mathrm{r}}$ is the infinitesimal area along which heat transfer occurs, α_r is the heat transfer coefficient between the tube and the refrigerant, T_T is the tube temperature, and T_r is the refrigerant temperature. Substituting Equation 3.6 and Equation 3.7 into Equation 3.5, dividing by $d\tilde{z}$, taking the limit as $d\tilde{z} \to 0$, and rearranging terms results in

$$A_{\mathrm{cs}}\frac{\partial}{\partial t}\left(\rho(\tilde{z},t)h(\tilde{z},t) - p(t)\right) + \frac{\partial}{\partial \tilde{z}}\left(\dot{m}(\tilde{z},t)h(\tilde{z},t)\right) = L_{\mathrm{r}}\alpha_{\mathrm{r}}\left(T_{\mathrm{t}}(\tilde{z},t) - T_{\mathrm{r}}(\tilde{z},t)\right). \tag{3.8}$$

Substituting $\tilde{z} = zL$ into Equation 3.8 results in

$$V\frac{\partial}{\partial t}\left(\rho(z,t)h(z,t) - p(t)\right) + \frac{\partial}{\partial z}\left(\dot{m}(z,t)h(z,t)\right) = A_{\mathrm{r}}\alpha_{\mathrm{r}}\left(T_{\mathrm{t}}(z,t) - T_{\mathrm{r}}(z,t)\right), \tag{3.9}$$

where A_{r} is the heat transfer area between the tube and the refrigerant.

3.1.3 Conservation of Energy - Air

As noted in [8], the air stores a negligible amount of energy, and the heat transfer coefficient α_{a} between the air and the tube is assumed to be constant across the entire heat transfer area A_{a}. The equation describing the air outlet temperature, $T_{\mathrm{a,out}}$, can thus be shown to be

$$T_{\mathrm{a,out}}(z,t) = T_{\mathrm{t}}(z,t) + \left(T_{\mathrm{a,in}}(t) - T_{\mathrm{t}}(z,t)\right)e^{-NTU(t)}, \tag{3.10}$$

where

$$NTU(t) = \frac{A_{\mathrm{a}}\alpha_{\mathrm{a}}}{\dot{m}_{\mathrm{a}}(t)c_{\mathrm{p,a}}}. \tag{3.11}$$

Note that since the air flowing into the evaporator is assumed to be uniform, the air inlet temperature, $T_{\mathrm{a,in}}$, and the air mass flow rate, $\dot{m}_{\mathrm{a}}$, are only functions of time and not of position. The air specific heat, $c_{\mathrm{p,a}}$, is assumed to be constant due to the negligible variation observed in the range of air temperatures present during operation.

3.1.4 Conservation of Energy - Tube

The energy balance for the tube is carried out via the first law of thermodynamics for a closed system by

$$\frac{dU_{\mathrm{t}}}{dt} = \dot{Q}_{\mathrm{r}} + \dot{Q}_{\mathrm{a}}, \tag{3.12}$$

where U_{t} is the internal energy of the tube, $\dot{Q}_{\mathrm{r}}$ is the heat transfer rate from the refrigerant to the tube, and $\dot{Q}_{\mathrm{a}}$ is the heat transfer rate from the air to the tube. The change in internal energy of the tube can be approximated from [5] by

$$dU_{\mathrm{t}} = m_{\mathrm{t}}c_{\mathrm{t}}dT_{\mathrm{t}}(z,t), \tag{3.13}$$

with m_{t} representing the mass of the tube and c_{t} representing the specific heat of the tube, which is assumed to be constant. The heat transfer rates are expressed as

$$\dot{Q}_{\mathrm{r}} = A_{\mathrm{r}}\alpha_{\mathrm{r}}\left(T_{\mathrm{r}}(z,t) - T_{\mathrm{t}}(z,t)\right) \tag{3.14}$$

and

$$\dot{Q}_{\mathrm{a}} = \dot{m}_{\mathrm{a}}(t)c_{\mathrm{p,a}}\left(T_{\mathrm{a,in}}(t) - T_{\mathrm{a,out}}(z,t)\right). \tag{3.15}$$

Substituting Equation 3.13, Equation 3.14, and Equation 3.15 into Equation 3.12

results in

$$m_{\mathrm{t}} c_{\mathrm{t}} \frac{\partial T_{\mathrm{t}}(z,t)}{\partial t} = A_{\mathrm{r}} \alpha_{\mathrm{r}} \left(T_{\mathrm{r}}(z,t) - T_{\mathrm{t}}(z,t) \right) + \dot{m}_{\mathrm{a}}(t) c_{\mathrm{p,a}} \left(T_{\mathrm{a,in}}(t) - T_{\mathrm{a,out}}(z,t) \right). \quad (3.16)$$

3.1.5 System Summary

Equation 3.3, Equation 3.9, Equation 3.10, and Equation 3.16 are derived by normalizing the length of the evaporator and applying conservation of mass and conservation of energy. These represent the set of continuous, nonlinear, partial differential equations (PDEs) used to model the evaporator dynamics.

Conservation of Mass - Refrigerant

$$V \frac{\partial}{\partial t} \rho(z,t) + \frac{\partial}{\partial z} \dot{m}(z,t) = 0 \quad (3.17a)$$

Conservation of Energy - Refrigerant

$$V \frac{\partial}{\partial t} \left(\rho(z,t) h(z,t) - p(t) \right) + \frac{\partial}{\partial z} \left(\dot{m}(z,t) h(z,t) \right) = A_{\mathrm{r}} \alpha_{\mathrm{r}} \left(T_{\mathrm{t}}(z,t) - T_{\mathrm{r}}(z,t) \right) \quad (3.17b)$$

Conservation of Energy - Air

$$T_{\mathrm{a,out}}(z,t) = T_{\mathrm{t}}(z,t) + \left(T_{\mathrm{a,in}}(t) - T_{\mathrm{t}}(z,t) \right) e^{-NTU(t)} \quad (3.17c)$$

Conservation of Energy - Tube

$$m_{\mathrm{t}} c_{\mathrm{t}} \frac{\partial T_{\mathrm{t}}(z,t)}{\partial t} = A_{\mathrm{r}} \alpha_{\mathrm{r}} \left(T_{\mathrm{r}}(z,t) - T_{\mathrm{t}}(z,t) \right) + \dot{m}_{\mathrm{a}}(t) c_{\mathrm{p,a}} \left(T_{\mathrm{a,in}}(t) - T_{\mathrm{a,out}}(z,t) \right) \quad (3.17d)$$

The refrigerant density and temperature will be estimated by the pressure and the specific enthalpy, and the initialization of Equation 3.17 is completed by implementing the initial and boundary conditions ([7], [9], [4]) shown in Table 3.1.

3.2 Finite Volume Discretization

In order to efficiently simulate the evaporator, Equation 3.17 will be discretized into N equal finite volumes, as described in [7]. The PDEs will be integrated over each

Table 3.1: Initial and Boundary Conditions for Evaporator PDE's

Initial Conditions	Boundary Conditions
$p(t=0) = p_0$	$\dot{m}(z=0,t) = \dot{m}_{\text{in}}(t)$
$h(z,t=0) = h_0(z)$	$\dot{m}(z=1,t) = \dot{m}_{\text{out}}(t)$
$\rho(z,t=0) = \rho_0(p_0, h_0(z))$	$h(z=0,t) = h_{\text{in}}(t)$
$T_{\text{r}}(z,t=0) = T_{\text{r},0}(p_0, h_0(z))$	$h(z=1,t) = h_{\text{out}}(t)$
$T_{\text{t}}(z,t=0) = T_{\text{t},0}(z)$	

volume and will be converted into ordinary differential equations that can easily be implemented in a simulation.

3.2.1 Refrigerant

The discretization will make use of an exact differential for the refrigerant density [5], expressed as

$$\frac{\partial}{\partial t}\rho(p(t), h(z,t)) = \frac{\partial}{\partial p}\rho(p,h)\Big|_h \frac{\mathrm{d}p}{\mathrm{d}t} + \frac{\partial}{\partial h}\rho(p,h)\Big|_p \frac{\mathrm{d}h}{\mathrm{d}t}, \tag{3.18}$$

where the subscripts h and p show that the specific enthalpy and the pressure, respectively, are held constant. Equation 3.18 is substituted into Equation 3.17a, and the equation is integrated over each of the control volumes to obtain

$$V \int_{z_{k-1}}^{z_k} \left(\frac{\partial}{\partial p}\rho \frac{\mathrm{d}p}{\mathrm{d}t} + \frac{\partial}{\partial h}\rho \frac{\mathrm{d}h}{\mathrm{d}t} \right) \mathrm{d}z + \int_{z_{k-1}}^{z_k} \frac{\partial}{\partial z}\dot{m}\, \mathrm{d}z = 0 \tag{3.19}$$

for $k = 1, ..., N$. Applying the midpoint rule [9] and the Upwind Differencing Scheme [11] results in

$$a_k \frac{\mathrm{d}p}{\mathrm{d}t} + b_k \frac{\mathrm{d}h_k}{\mathrm{d}t} = \dot{m}_{k-1} - \dot{m}_k, \tag{3.20}$$

with

$$a_k = V_k \frac{\partial}{\partial p} \rho_{p,k}, \tag{3.21}$$

$$b_k = V_k \frac{\partial}{\partial h} \rho_{h_k,k}, \tag{3.22}$$

$$\rho_{p,k} = \frac{1}{z_k - z_{k-1}} \int_{z_{k-1}}^{z_k} \frac{\partial}{\partial p} \rho \, \mathrm{d}z, \tag{3.23}$$

$$\rho_{h_k,k} = \frac{1}{z_k - z_{k-1}} \int_{z_{k-1}}^{z_k} \frac{\partial}{\partial h_k} \rho \, \mathrm{d}z, \tag{3.24}$$

and

$$h_k = \frac{1}{z_k - z_{k-1}} \int_{z_{k-1}}^{z_k} h \, \mathrm{d}z, \tag{3.25}$$

where $\dot{m}_{k-1}$ is the refrigerant mass flow rate into the k^{th} volume, and $\dot{m}_k$ is the refrigerant mass flow rate out of the k^{th} volume.

The same procedure can be applied to Equation 3.17b to obtain

$$\begin{aligned} &V \int_{z_{k-1}}^{z_k} \left(h \frac{\partial}{\partial p} \rho - 1 \right) \frac{\mathrm{d}p}{\mathrm{d}t} + \left(h \frac{\partial}{\partial h} \rho + \rho \right) \frac{\mathrm{d}h}{\mathrm{d}t} \mathrm{d}z + \int_{z_{k-1}}^{z_k} \frac{\partial}{\partial z} \left(\dot{m} h \right) \mathrm{d}z \\ &= \int_{z_{k-1}}^{z_k} A_{\mathrm{r}} \alpha_{\mathrm{r}} \left(T_{\mathrm{t}}(z,t) - T_{\mathrm{r}}(z,t) \right) \mathrm{d}z, \end{aligned} \tag{3.26}$$

which can then be written as

$$c_k \frac{\mathrm{d}p}{\mathrm{d}t} + d_k \frac{\mathrm{d}h_k}{\mathrm{d}t} = \dot{m}_{k-1} h_{k-1} - \dot{m}_k h_k - A_{\mathrm{r},k} \alpha_{\mathrm{r}} \left(T_{\mathrm{r},k} - T_{\mathrm{t},k} \right), \tag{3.27}$$

with

$$c_k = V_k \left(h_k \frac{\partial}{\partial p} \rho_{p,k} - 1 \right), \tag{3.28}$$

$$d_k = V_k \left(h_k \frac{\partial}{\partial h} \rho_{h_k,k} + \rho_k \right), \tag{3.29}$$

and

$$\rho_k = \frac{1}{z_k - z_{k-1}} \int_{z_{k-1}}^{z_k} \rho \, \mathrm{d}z. \tag{3.30}$$

For brevity, the heat transfer rate from the refrigerant to the tube for the k^{th} control volume will be written as

$$\dot{Q}_{\mathrm{r},k} = A_{\mathrm{r},k} \alpha_{\mathrm{r}} \left(T_{\mathrm{r},k} - T_{\mathrm{t},k} \right). \tag{3.31}$$

The mass and energy balances presented yield $2N$ equations with $2N$ unknowns: the refrigerant pressure, the refrigerant specific enthalpy of each control volume, and the mass flow rates between each control volume. As in [7] and [4], the intermediate mass flow rates can be algebraically eliminated to reduce the computational complexity of the model. Utilizing Equation 3.20, the k^{th} mass flow rate is

$$\dot{m}_k = \dot{m}_{k-1} - a_k \frac{\mathrm{d}p}{\mathrm{d}t} - b_k \frac{\mathrm{d}h_k}{\mathrm{d}t}, \tag{3.32}$$

which can be plugged into Equation 3.27 to obtain

$$\left(c_k - a_k h_k \right) \frac{\mathrm{d}p}{\mathrm{d}t} + \left(d_k - b_k h_k \right) \frac{\mathrm{d}h_k}{\mathrm{d}t} = \dot{m}_{k-1} \left(h_{k-1} - h_k \right) - \dot{Q}_{\mathrm{r},k}. \tag{3.33}$$

The mass flow rate out of the k^{th} volume can be recursively determined by

$$\dot{m}_k = \dot{m}_{\mathrm{in}} - \sum_{i=1}^{k} \left(a_i \frac{\mathrm{d}p}{\mathrm{d}t} + b_i \frac{\mathrm{d}h_i}{\mathrm{d}t} \right), \tag{3.34}$$

which can be adapted for $\dot{m}_{k-1}$ and plugged into Equation 3.33, resulting in

$$\begin{aligned} \left(c_k - a_k h_k + \left(h_{k-1} - h_k \right) \sum_{i=1}^{k-1} a_i \right) \frac{\mathrm{d}p}{\mathrm{d}t} + \left(d_k - b_k h_k \right) \frac{\mathrm{d}h_k}{\mathrm{d}t} + \left(h_{k-1} - h_k \right) \sum_{i=1}^{k-1} \left(b_i \frac{\mathrm{d}h_i}{\mathrm{d}t} \right) \\ = \dot{m}_{\mathrm{in}} (h_{k-1} - h_k) - \dot{Q}_{\mathrm{r},k}. \end{aligned} \tag{3.35}$$

Equation 3.32 and Equation 3.33 can be summed over all N volumes to obtain

$$\left(\sum_{i=1}^{N} a_i\right)\frac{\mathrm{d}p}{\mathrm{d}t} + \left(\sum_{i=1}^{N} b_i \frac{\mathrm{d}h_i}{\mathrm{d}t}\right) = \dot{m}_{\mathrm{in}} - \dot{m}_{\mathrm{out}} \tag{3.36}$$

and

$$\left(\sum_{i=1}^{N} c_i\right)\frac{\mathrm{d}p}{\mathrm{d}t} + \left(\sum_{i=1}^{N} d_i \frac{\mathrm{d}h_i}{\mathrm{d}t}\right) = \dot{m}_{\mathrm{in}} h_{\mathrm{in}} - \dot{m}_{\mathrm{out}} h_{\mathrm{out}} - \sum_{i=1}^{N} \dot{Q}_{\mathrm{r},i}, \tag{3.37}$$

which can be combined with Equation 3.35 for $k = 1, ..., N-1$ to obtain $N+1$ equations for the $N+1$ unknowns, the rates of change of the refrigerant pressure in the evaporator and of the refrigerant specific enthalpies within each control volume. The equations can be expressed compactly in matrix form as

$$A\dot{X} = B, \tag{3.38}$$

where

$$X = \left[p, h_1, h_2, \cdots, h_N\right]^T, \tag{3.39}$$

$$A = \begin{bmatrix} \sum_{i=1}^{N} a_i & b_1 & b_2 & \cdots & \cdots & \cdots & \cdots & \cdots & b_N \\ \sum_{i=1}^{N} c_i & d_1 & d_2 & \cdots & \cdots & \cdots & \cdots & \cdots & d_N \\ e_1 & g_1 & 0 & \cdots & \cdots & \cdots & \cdots & \cdots & 0 \\ s_2 & b_1 r_2 & g_2 & 0 & \cdots & \cdots & \cdots & \cdots & 0 \\ s_3 & b_1 r_3 & b_2 r_3 & g_3 & 0 & \cdots & \cdots & \cdots & 0 \\ \vdots & \vdots & \vdots & \vdots & \ddots & \ddots & & & \vdots \\ \vdots & \vdots & \vdots & \vdots & & \ddots & \ddots & & \vdots \\ \vdots & \vdots & \vdots & \vdots & & & \ddots & \ddots & \vdots \\ s_{N-1} & b_1 r_{N-1} & b_2 r_{N-1} & b_3 r_{N-1} & \cdots & \cdots & \cdots & g_n & 0 \end{bmatrix}, \tag{3.40}$$

$$e_i = c_i - a_i h_i, g_i = d_i - b_i h_i,$$

$$s_i = e_i - (h_i - h_{i-1}) \sum_{j=1}^{i-1} a_j, r_i = h_{i-1} - h_i,$$

and

$$B = \begin{bmatrix} \dot{m}_{\text{in}} - \dot{m}_{\text{out}} \\ \dot{m}_{\text{in}} h_{\text{in}} - \dot{m}_{\text{out}} h_{\text{out}} - \sum_{i=1}^{N} \dot{Q}_{\text{r},i} \\ \dot{m}_{\text{in}} (h_{\text{in}} - h_1) - \dot{Q}_{\text{r},1} \\ \dot{m}_{\text{in}} (h_1 - h_2) - \dot{Q}_{\text{r},2} \\ \vdots \\ \dot{m}_{\text{in}} (h_{N-2} - h_{N-1}) - \dot{Q}_{\text{r},N-1} \end{bmatrix}. \tag{3.41}$$

3.2.2 Air

Integrating Equation 3.17c over the k^{th} volume results in

$$\int_{z_{k-1}}^{z_k} T_{\text{a,out}} \mathrm{d}z = \int_{z_{k-1}}^{z_k} T_{\text{t}} + (T_{\text{a,in}} - T_{\text{t}})\, e^{-NTU} \mathrm{d}z, \tag{3.42}$$

which can be approximated using the same method from subsection 3.2.1 to obtain

$$T_{\text{a,out},k} = T_{\text{t},k} + (T_{\text{a,in}} - T_{\text{t},k})\, e^{-NTU,k}. \tag{3.43}$$

As with h_k and ρ_k in Section subsection 3.2.1, $T_{\text{a,out},k}$ and $T_{\text{t},k}$ represent the average air outlet temperature and average tube temperature, respectively, for the k^{th} volume. The discretized exponential term in Equation 3.43 is written as

$$NTU, k = \frac{A_{\text{a},k}\alpha_{\text{a}}}{\dot{m}_{\text{a},k} c_{\text{p,a}}}. \tag{3.44}$$

As with h_k and ρ_k in subsection 3.2.1, $T_{\text{a,out},k}$ and $T_{\text{t},k}$ represent the average air outlet temperature and average tube temperature, respectively, for the k^{th} volume. The air inlet term, $T_{\text{a,in}}$, remains unchanged due to the assumption in section 3.1 regarding the uniform airflow into the evaporator. The overall air outlet temperature is calculated as the average of the N individual air outlet temperatures and is expressed as

$$T_{\text{a,out}} = \frac{1}{N} \sum_{i=1}^{N} T_{\text{a,out},k}. \tag{3.45}$$

3.2.3 Tube

In the same manner, Equation 3.17d can be integrated over the k^{th} volume to obtain

$$\int_{z_{k-1}}^{z_k} m_{\text{t}} c_{\text{t}} \frac{\partial T_{\text{t}}}{\partial t} \mathrm{d}z = \int_{z_{k-1}}^{z_k} A_{\text{r}} \alpha_{\text{r}} (T_{\text{r}} - T_{\text{t}}) + \dot{m}_{\text{a}} c_{\text{p,a}} (T_{\text{a,in}} - T_{\text{a,out}} \mathrm{d}z) \tag{3.46}$$

and approximated as

$$m_{\mathrm{t},k} c_{\mathrm{t}} \frac{\partial T_{\mathrm{t},k}}{\partial t} = \dot{Q}_{\mathrm{r},k} + \dot{Q}_{\mathrm{a},k}, \tag{3.47}$$

where $\dot{Q}_{\mathrm{r},k}$ is defined in Equation 3.31, and

$$\dot{Q}_{\mathrm{a},k} = \dot{m}_{\mathrm{a},k} c_{\mathrm{p,a}} \left(T_{\mathrm{a,in}} - T_{\mathrm{a,out},k} \right). \tag{3.48}$$

3.3 Parameter Identification

For the simulation, the state vector will be considered as

$$x = \left[p, h_1, h_2, \cdots, h_N, T_{\mathrm{t},1}, T_{\mathrm{t},2}, \cdots, T_{\mathrm{t},N} \right]^T. \tag{3.49}$$

Use of the model requires knowledge of the system parameters $\alpha_{\mathrm{r}}, A_{\mathrm{r}}, \alpha_{\mathrm{a}}, A_{\mathrm{a}}, m_{\mathrm{t}}$, and V, which are determined via simulation within MATLAB and Simulink by comparing the model results to measurement data recorded at a test bench. Since the system behaves in a stiff manner [4], the solver ode23tb is used to run each simulation. As in [9], the heat transfer coefficients can be approximated as a linear function of either air or refrigerant mass flow rate:

$$\alpha = a + b\dot{m}. \tag{3.50}$$

As noted in [4], the air and refrigerant heat transfer areas only appear as products with their respective heat transfer coefficients, so Equation 3.50 is extended to include the areas:

$$A_{\mathrm{r}} \alpha_{\mathrm{r}} = a_{\mathrm{r}} + b_{\mathrm{r}} \dot{m}, \tag{3.51}$$

$$A_{\mathrm{a}}\alpha_{\mathrm{a}} = a_{\mathrm{a}} + b_{\mathrm{a}}\dot{m}_{\mathrm{a}}. \tag{3.52}$$

In order to get the initial conditions for the h_1 through h_N, the specific enthalpy profile is assumed to be linear, so each value is interpolated from the measured inlet and outlet specific enthalpies. A similar process is performed for the tube temperatures, except that the first and last tube temperatures will be added as parameters that need to be determined [4]. The simulated pressure tracks the measured pressure with the use of a P-controller to adjust the outlet refrigerant mass flow rate since this flow rate is not measured. The parameters are estimated by minimizing the sum of the squared percent errors between the measured and simulated pressures, outlet specific enthalpies, and air outlet temperatures, expressed as

$$\min_{a_r,b_r,a_a,b_a,m_T,V} \sum_{t=T_{\mathrm{Start}}}^{T_{\mathrm{End}}} K_{\mathrm{pr}}e_{\mathrm{pr}}^2 + \ K_{\mathrm{h}}e_{\mathrm{h}}^2 + K_{\mathrm{a}}e_{\mathrm{a}}^2, \tag{3.53}$$

$$e_{\mathrm{pr}} = \left(\frac{p_{\mathrm{sim}}(t) - p_{\mathrm{meas}}(t)}{\max\left(p_{\mathrm{meas}}(t)\right)}\right), \tag{3.54}$$

$$e_{\mathrm{h}} = \left(\frac{h_{\mathrm{out,sim}}(t) - h_{\mathrm{out,meas}}(t)}{\max\left(h_{\mathrm{out,meas}}(t)\right)}\right), \tag{3.55}$$

$$e_{\mathrm{a}} = \left(\frac{T_{\mathrm{a,out,sim}}(t) - T_{\mathrm{a,out,meas}}(t)}{\max\left(T_{\mathrm{a,out,meas}}(t)\right)}\right). \tag{3.56}$$

The use of the maximum measured values allows for scaling to adjust for the difference in the units between the three outputs, and the positive constants $K_{\mathrm{pr}}, K_{\mathrm{h}}$, and K_{t} allow for manual weighting of the outputs that can be adjusted depending on which outputs are most important for a given application.

3.4 Model Validation

The model validation is performed by simulating the system with the identified parameters and comparing the outputs with measured output values gathered from a test bench. The inputs into the simulation, $T_{\mathrm{a,in}}$, $\dot{m}_{\mathrm{air}}$, h_{in}, and $\dot{m}_{\mathrm{r,in}}$, are taken from the measured values, and the performance of the model is measured by the mean percent error (MPE) of each output of the simulation from the model, represented as

$$MPE = \sum_{i=1}^{N_{\mathrm{p}}} \frac{\mid val_{\mathrm{sim}}(i) - val_{\mathrm{meas}}(i) \mid}{val_{\mathrm{meas}}(i)} \cdot \frac{100}{N_{\mathrm{p}}}, \tag{3.57}$$

where N_{p} is the number of data points in the set, and val represents the value of the output variable. The results from four validation tests are shown in Table 3.2. The plot of Validation 1 is shown in Figure 3.2, and the rest of the validation test plots are in the appendix in Figure 6.1 - Figure 6.3.

Table 3.2: Mean percent errors for each validation test

Trial	Validation 1	Validation 2	Validation 3	Validation 4
p	$1.56 \times 10^{-3}\,\%$	$2.93 \times 10^{-3}\,\%$	$1.36 \times 10^{-3}\,\%$	$2.54 \times 10^{-3}\,\%$
h_{out}	$5.04\,\%$	$3.95\,\%$	$9.98\,\%$	$6.57\,\%$
$T_{\mathrm{a,out}}$	$2.04\,\%$	$3.86\,\%$	$1.21\,\%$	$1.73\,\%$

As can be seen in Table 3.2 and in Figure 3.2, the simulation produces an accurate prediction of the pressure. This is due to the P-controller that is implemented to control the refrigerant outlet mass flow rate. While this controller produces excellent results for the pressure, the lack of measurement of the outlet mass flow rate may have led to errors elsewhere in the simulation, especially with the refrigerant enthalpy. The enthalpy may also be affected by the assumptions of a linear tube temperature profile due to the interdependence between the tube temperatures and the refrigerant temperatures. Additionally, as noted in [7], the refrigerant enthalpy profile for each phase could be assumed to be exponential rather than linear as was assumed in this

work. Further investigation is necessary to determine if the exponential profile would produce more accurate results than the linear profile.

Since the refrigerant temperature profile is not linear anytime there are at least two phases in the evaporator, this may cause a nonlinear tube temperature profile, which can also cause errors in the air outlet temperatures. The simulated air outlet temperatures in Figure 3.2 and Figure 6.1 tend to be higher than the measured temperatures, whereas the temperature errors in Figure 6.2 and Figure 6.3 show more variance in direction. This may be caused by inconsistent or insufficient mixing of the air coming out of each finite volume. Air coming out of the first finite volume would be hotter than air coming out of the last finite volume, so if the air is not completely mixed and its flow changes, this could cause the temperature sensors' readings to change even if the average temperature of all N volumes does not change. A potential solution would be to move the temperature sensors slightly further away from the evaporator to allow more space for mixing, but the temperature estimation is sufficiently accurate for the required application.

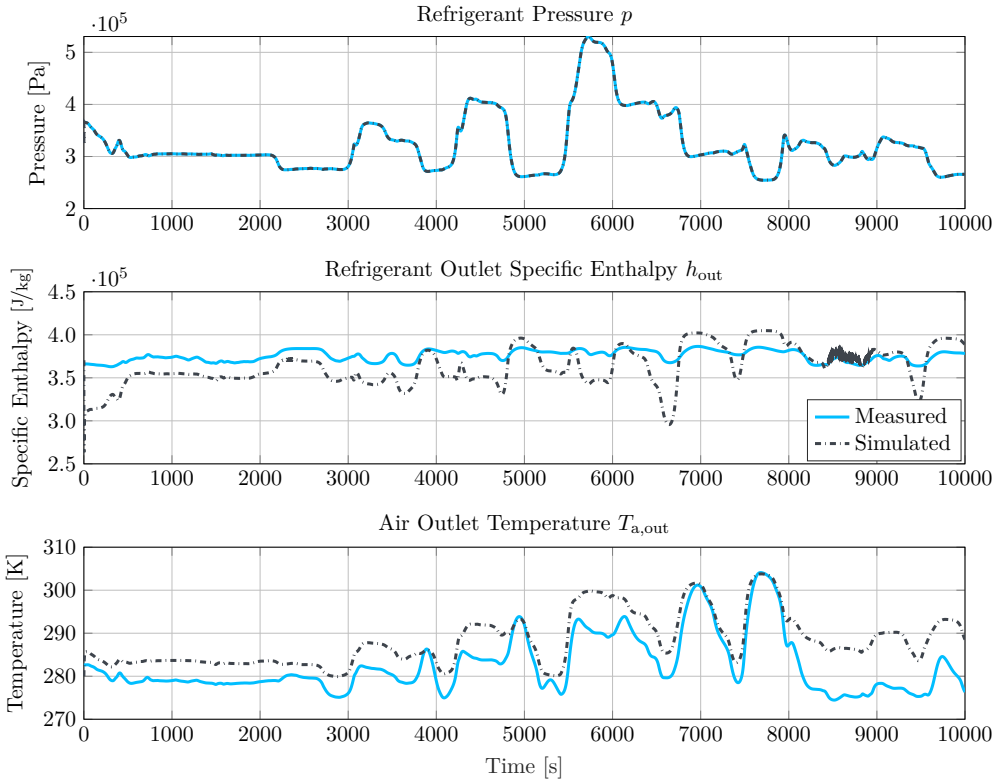

Figure 3.2: Results from validation 1.

CHAPTER 4

CONTROLLER DESIGN

Vapor compression systems are controlled with a wide variety of strategies. For example, [12] discusses the use of online model predictive control (MPC) for the regulation of refrigeration capacity, which corresponds to water temperature. Two controllers are developed: one uses only the coefficient of performance (which corresponds to the compressor speed) as the input, and the other uses the coefficient of performance and evaporator and condenser refrigerant mass flow rates as the inputs. The MPCs developed balance the water temperature error with the compressor speed and rate of change, and the second MPC adds a term that penalizes refrigerant mass flow rates outside of a predetermined interval. The superheating for the refrigerant leaving the evaporator is controlled via proportional-integral-derivative (PID) control. Both controllers increase the coefficient of performance, thus showing the viability of MPC for vapor compression cycles. It must be noted, however, that the use of online MPC may prove computationally difficult, so care must be taken to ensure the controller hardware can perform quickly enough.

The work in [13] presents a reduced order H_∞ controller based off of the MPC design from [12]. The goal of the controller is to track the desired pressure difference between the condenser and the evaporator, which corresponds to the system output temperature, and the desired refrigerant superheating, which corresponds to the controller efficiency. While tracking, the controller must also reject disturbances. The controller presented succeeds in both of these tasks, but no discussion is given regarding the performance compared to other controllers.

PID and frequency domain control can also be used to control AC systems, as demonstrated in [14]. The controllers presented are designed to control the evapora-

tor refrigerant superheat and the evaporator secondary fluid temperature using the compressor speed and the expansion valve opening as inputs. Even in the presence of disturbances, both controller succeed, and the PID controller outperforms the transfer function-based controller.

This work aims to explore the validity of a sliding mode controller (SMC) for the control of the evaporator since sliding mode control provides robustness to disturbances and model uncertainties ([15], [16]). The system will be controlled by two separate controllers whose performances will be compared. The first will be a single-input single-output (SISO) sliding mode controller (SMC), and the second will be a PID controller. Both will control the air outlet temperature via the refrigerant inlet mass flow rate, and a PI controller implemented in the same way as the P controller in Chapter chapter 3 will control the refrigerant pressure via the outlet mass flow rate. Controlling the refrigerant pressure prevents the test bench from shutting down for safety reasons if the pressure becomes too low.

This chapter discusses the general design of a proportional-integral-derivative (PID) controller and of a SISO sliding mode controller and how they are applied to the evaporator. In order to properly implement the controllers within a physical system, the expansion valve (EXV) and the compressor models are added, and the relationships between the desired refrigerant mass flow rates and the EXV and compressor inputs are examined. The controller performances for each controller are then simulated for various operating points and transitions.

4.1 General Design for PID Control

PID controllers are used for a wide variety of systems, linear and nonlinear alike. The general setup of a PID controller is shown in Figure 4.1. The K_{P}, K_{I}, and K_{D} terms represent the weights for the proportional, integral, and derivative terms, respectively. The output error e_{y} is determined by the difference between the desired output y_{d}

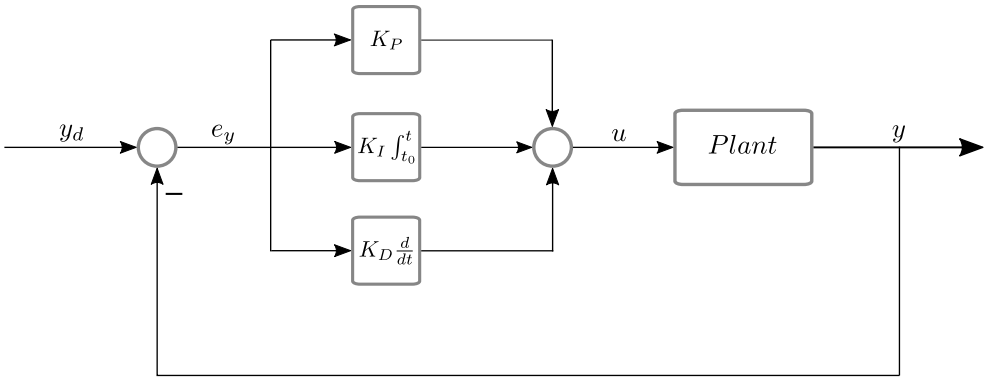

Figure 4.1: General PID controller diagram [17].

and the system output y and is then used to solve for the input u through

$$u(t) = K_{\mathrm{P}} \cdot e_{\mathrm{y}}(t) + K_{\mathrm{I}} \int_{t_0}^{t} e_{\mathrm{y}}(\tau)\mathrm{d}\tau + K_{\mathrm{D}} \frac{\mathrm{d}e_{\mathrm{y}}}{\mathrm{d}t}. \tag{4.1}$$

The proportional term largely determines the speed with which the output approaches the desired value. As K_{P} increases, the system response speed increases. Care must be taken, however, as at large enough values, the proportional term can cause excessive oscillation or even instability [18].

The integral term acts to eliminate steady state error. The most common issue arising from the use of integral control results from error windup, which results from the system being unable to reduce the error for an extended period of time. This can also cause excessive oscillation or instability and can result from issues such as actuator saturation [17].

The derivative term acts as damper to the system response and prevents overshoot by reducing the magnitude of the input when the system output is changing rapidly. Noise in the system, however, can significantly amplify the derivative term and cause undesired behavior in the system response [17].

The PI and PID controllers implemented for the evaporator are manually tuned in Simulink with the continuous-time PID Controller block. The block utilizes clamping to prevent error windup and a filter for the derivative to reduce the noise.

4.2 General Design for SISO Sliding Mode Control

A nonlinear SISO input-affine system can be defined as

$$\begin{aligned} \dot{x} &= f(x,t) + g(x,t) \cdot u \\ y &= h(x,t) \end{aligned} \tag{4.2}$$

where $x \in \mathbb{R}^n$ is the state vector, $u \in \mathbb{R}$ is the input, $y \in \mathbb{R}$ is the output, $f(x,t) \in \mathbb{R}^n$, $g(x,t) \in \mathbb{R}^n$, and $h(x,t) \in \mathbb{R}$. For such a system, a sliding surface [16] can be defined based on [15] as

$$s = \sum_{j=0}^{r-1} \lambda_j \left(y - y_{\mathrm{d}}\right)^{(j)} = \sum_{j=0}^{r-1} \lambda_j e_{\mathrm{y}}^{(j)}, \tag{4.3}$$

where r is the relative degree of the output, λ_j represents a constant to be chosen by the designer, y_{d} is the desired output, and $e_{\mathrm{y}}^{(j)}$ is the j^{th} time derivative of the output error. Each λ_j is chosen such that the polynomial

$$\lambda_0 + \lambda_1 p + \lambda_2 p^2 + \cdots + \lambda_{r-1} p^{r-1} = 0, \tag{4.4}$$

is Hurwitz, i.e., each root of Equation 4.4 has negative real part [19]. The relative degree is found by taking the time derivative of the output until there is a direct dependence on the input. The first derivative is expressed as

$$\dot{y} = \frac{\partial h(x,t)}{\partial t} + L_f h + L_g h \cdot u, \tag{4.5}$$

$$L_f h = \frac{\partial h(x,t)}{\partial x} f(x,t), \tag{4.6}$$

$$L_g h = \frac{\partial h(x,t)}{\partial x} g(x,t), \tag{4.7}$$

where $L_f h$ and $L_g h$ are referred to as Lie Derivatives [20]. For a relative degree greater than one, Equation 4.7 will be equal to zero, so another time derivative is necessary. The output's j^{th} time derivative is shown as

$$y^{(j)} = \frac{\partial^j h(x,t)}{\partial t^j} + L_f^j h + L_g L_f^{j-1} h \cdot u, \tag{4.8}$$

$$L_f^j h = L_f L_f^{j-1} h, \tag{4.9}$$

$$L_g L_f^{j-1} h = \frac{\partial L_f^{j-1} h}{\partial x} g(x,t), \tag{4.10}$$

$$L_f^0 h = h(x,t). \tag{4.11}$$

If Equation 4.10 is non-zero, then $r = j$, and Equation 4.10 will equal zero for each $j < r$. In order to bring the system onto the sliding surface, i.e., zero output error, a control law will be defined based on Lyapunov's theorem [20]. The surface is shown to be asymptotically stable if there exists a Lyapounov function $V(s)$ such that

$$V(s) > 0 \quad \forall\ s \neq 0, \tag{4.12}$$

$$V(0) = 0, \tag{4.13}$$

$$\dot{V}(s) < 0 \quad \forall\ s \neq 0. \tag{4.14}$$

Defining a Lyapunov candidate as

$$V(s) = \frac{1}{2}s^2, \tag{4.15}$$

the time derivative is calculated as

$$\dot{V}(s) = \frac{\partial V}{\partial t} + \frac{\partial V}{\partial s}\frac{\mathrm{d}s}{\mathrm{d}t} = s\dot{s}. \tag{4.16}$$

From Equation 4.3, $\dot{s}$ is shown to be

$$\begin{aligned} \dot{s} &= \sum_{j=0}^{r-1} \lambda_j \left(\frac{\partial e_y^{(j)}}{\partial t} + \frac{\partial e_y^{(j)}}{\partial x}\dot{x} \right) \\ &= \sum_{j=0}^{r-1} \lambda_j \left(\frac{\partial e_y^{(j)}}{\partial t} + \frac{\partial e_y^{(j)}}{\partial x} f + \frac{\partial e_y^{(j)}}{\partial x} g \cdot u \right) \\ &= h + b \cdot u, \end{aligned} \tag{4.17}$$

where

$$h = \sum_{j=0}^{r-1} \lambda_j \left(\frac{\partial e_y^{(j)}}{\partial t} + \frac{\partial e_y^{(j)}}{\partial x} f \right), \tag{4.18}$$

$$b = \sum_{j=0}^{r-1} \lambda_j \left(\frac{\partial e_y^{(j)}}{\partial x} g \right). \tag{4.19}$$

Defining the control law as

$$u = -\frac{1}{b}\left(h + k \cdot \mathrm{sign}(s)\right), \tag{4.20}$$

where b is invertible, and k is a positive constant. Plugging Equation 4.17 and Equation 4.20 into Equation 4.16 and simplifying results in

$$\dot{V}(s) = -ks \cdot \mathrm{sign}(s) = -k|s|, \tag{4.21}$$

which is less than zero for all $s \neq 0$. The conditions from Equation 4.12 - Equation 4.14 are fulfilled, and thus, the sliding surface s is asymptotically stable. In practice, however, the control law in Equation 4.20 will cause rapid control switching, known as chattering, within the system ([21], [16]). One method to mitigate this is to replace the sign function with a saturation function ([16], [15]), defined as

$$\text{sat}(s) = \begin{cases} \text{sign} & if|s| > \phi \\ \\ \frac{s}{\phi} & if|s| \leq \phi \end{cases}, \tag{4.22}$$

where ϕ corresponds to the boundary layer thickness [21]. The boundary layer helps prevent the controller from overshooting the sliding surface, and the control law Equation 4.20 can be rewritten as

$$u = \frac{1}{b}\left(h + k \cdot \text{sat}(s)\right). \tag{4.23}$$

The new control law Equation 4.23 can be proven in the same manner used for Equation 4.20 to make the sliding surface asymptotically stable. For $r < n$, the stability of the internal dynamics needs to be analyzed as well. The method presented here will be used in the next section to develop a controller for the evaporator.

4.3 Controller Design for Evaporator

The SMC control design presented in section 4.2 can easily be adapted to the evaporator used. The controller will then be paired with a PI controller to produce an overall plant with inputs $\dot{m}_{\text{in}}$ and $\dot{m}_{\text{out}}$ and outputs p and $T_{\text{a,out}}$.

4.3.1 SMC Design

In order to proceed with the design, the sliding surface must be defined. To do so, the output is defined from Chapter 3 as

$$y = T_{\mathrm{a,out}} = \frac{1}{N}\sum_{k=1}^{N} T_{\mathrm{a,out},k}, \tag{4.24}$$

where

$$T_{\mathrm{a,out},k} = \left(T_{\mathrm{t},k} + \left(T_{\mathrm{a,in}} - T_{\mathrm{t},k}\right)\mathrm{e}^{-NTU,k}\right). \tag{4.25}$$

The output equation can be simplified significantly by looking into the NTU term in Equation 4.25:

$$NTU, k = \frac{A_{\mathrm{a},k}\alpha_{\mathrm{a}}}{\dot{m}_{\mathrm{a},k}c_{\mathrm{p,a}}} = \frac{a_{\mathrm{a}} + b_{\mathrm{a}}\frac{\dot{m}_{\mathrm{a}}}{N}}{\dot{m}_{\mathrm{a}}c_{\mathrm{p,a}}}. \tag{4.26}$$

Using the values obtained from the parameter identification for a_{a} and b_{a} and assuming $\dot{m}_{\mathrm{a}} \in [1e^{-3}, 0.2]\,{}^{\mathrm{kg}}/_{\mathrm{s}}$, the values of e^{-NTU} over the air mass flow rate operating range are shown in Figure 4.2 for $N = 20$. As can be seen from the plot, e^{-NTU} is negligible for the entire operating range, and it can be confirmed that this holds true for any value of N that may be used for the model. The output can therefore be simplified to

$$y = \frac{1}{N}\sum_{k=1}^{N} T_{\mathrm{a,out},k} = \frac{1}{N}\sum_{k=1}^{N} T_{\mathrm{t},k}, \tag{4.27}$$

with a first time derivative of

$$\dot{y} = \frac{1}{N}\sum_{k=1}^{N} \frac{\left(a_{\mathrm{r}} + b_{\mathrm{r}}\frac{\dot{m}_{\mathrm{in}}+\dot{m}_{\mathrm{out}}}{2}\right)\left(T_{\mathrm{r},k} - T_{\mathrm{t},k}\right) + \dot{Q}_{\mathrm{a},k}}{m_{\mathrm{t}}c_{\mathrm{t}}}, \tag{4.28}$$

$$\dot{Q}_{\mathrm{a},k} = \dot{m}_{\mathrm{a},k}c_{\mathrm{p,a}}\left(T_{\mathrm{a,in}} - T_{\mathrm{a,out},k}\right). \tag{4.29}$$

Recalling that for the SMC, $u = \dot{m}_{\mathrm{in}}$, so equation Equation 4.28 can be rearranged

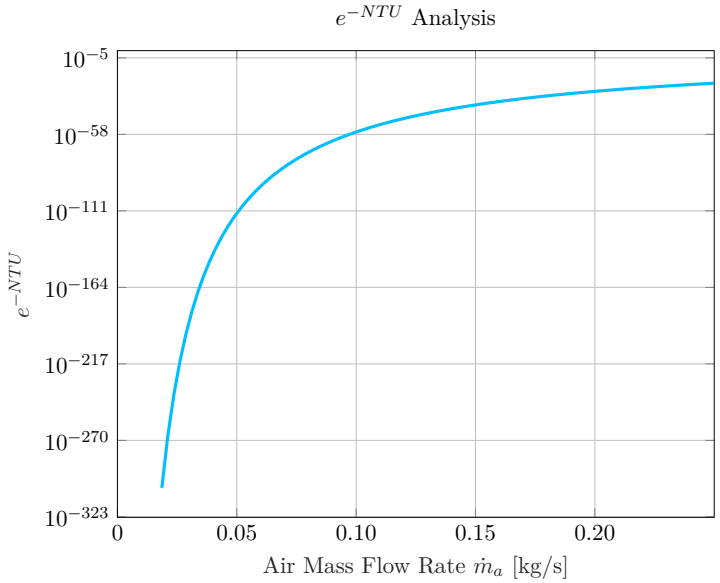

Figure 4.2: e^{-NTU} vs. air mass flow rate for $N = 20$.

into

$$\dot{y} = \frac{1}{N}\sum_{k=1}^{N} \frac{\left(a_{\mathrm{r}} + b_{\mathrm{r}}\frac{\dot{m}_{\mathrm{out}}}{2}\right)\left(T_{\mathrm{r},k} - T_{\mathrm{t},k}\right) + \dot{Q}_{\mathrm{a},k}}{m_t c_t} + \frac{1}{N}\sum_{k=1}^{N} \frac{b_{\mathrm{r}}\left(T_{\mathrm{r},k} - T_{\mathrm{t},k}\right)}{2m_{\mathrm{t}}c_{\mathrm{t}}} \cdot u, \tag{4.30}$$

and the output is thus shown to have relative degree $r = 1$. The sliding surface is then defined from equation Equation 4.3 as

$$s = y - y_{\mathrm{d}} = T_{\mathrm{a,out}} - T_{\mathrm{a,out,d}}. \tag{4.31}$$

During operation of the system, the desired output temperature is assumed to operate in a step-wise manner, so its time derivative will be zero unless the desired temperature is changed. Although the change will cause a non-zero time derivative, the derivative will almost instantaneously go back to zero, so for simplicity, the time derivative of the desired output will be assumed to zero at all times. The time derivative of the sliding surface is now equal to that of the output, so, using the

method from section 4.2, the input is defined as

$$u = -\frac{1}{b}\left(h + k \cdot \mathrm{sat}(T_{\mathrm{a,out}} - T_{\mathrm{a,out,d}})\right), \tag{4.32}$$

$$b = \sum_{k=1}^{N} \frac{b_{\mathrm{r}}\left(T_{\mathrm{r},k} - T_{\mathrm{t},k}\right)}{2 m_{\mathrm{t}} c_{\mathrm{t}}}, \tag{4.33}$$

$$h = \sum_{k=1}^{N} \frac{\left(a_{\mathrm{r}} + b_{\mathrm{r}} \frac{\dot{m}_{\mathrm{out}}}{2}\right)\left(T_{\mathrm{r},k} - T_{\mathrm{t},k}\right) + \dot{Q}_{\mathrm{a},k}}{m_{\mathrm{t}} c_{\mathrm{t}}}. \tag{4.34}$$

Since the relative degree of the output is less than the system order, the stability of the internal dynamics must be checked by analyzing the zero dynamics [22].

4.3.2 Zero Dynamics

The zero dynamics represent the behavior of the internal dynamics of the system when the output is brought to zero. In order to analyze these dynamics, the internal dynamics must first be selected, and this will be done using a method from [22]. For a system with output relative degree $r < n$, the state equations can be transformed via

$$\Phi(x) = \begin{bmatrix} \Phi_1(x) \\ \Phi_2(x) \\ \vdots \\ \Phi_r(x) \\ \Phi_{r+1}(x) \\ \vdots \\ \Phi_n(x) \end{bmatrix} = \begin{bmatrix} y \\ \dot{y} \\ \vdots \\ y^{(r-1)} \\ \Phi_{r+1}(x) \\ \vdots \\ \Phi_n(x) \end{bmatrix}, \tag{4.35}$$

where $\Phi_{r+1}(x)$ through $\Phi_n(x)$ represent the internal dynamics and are chosen so that the Jacobian of $\Phi(x)$ has full rank and is thus invertible. Applying this to the

evaporator SMC results in

$$\Phi(x) = \begin{bmatrix} \frac{1}{N}\sum_{k=1}^{N} T_{\mathrm{t},k} \\ \Phi_2(x) \\ \vdots \\ \Phi_n(x) \end{bmatrix}, \tag{4.36}$$

$$\frac{\partial \Phi}{\partial x} = \begin{bmatrix} 0 & 0 & \cdots & 0 & \frac{1}{N}T_{\mathrm{t},1} & \cdots & \frac{1}{N}T_{\mathrm{t},N} \\ \frac{\partial \Phi_2}{\partial p} & \frac{\partial \Phi_2}{\partial h_1} & \cdots & \frac{\partial \Phi_2}{\partial h_N} & \frac{\partial \Phi_2}{\partial T_{\mathrm{t},1}} & \cdots & \frac{\partial \Phi_2}{\partial T_{\mathrm{t},N}} \\ \vdots & \vdots & & \vdots & \vdots & & \vdots \\ \vdots & \vdots & & \vdots & \vdots & & \vdots \\ \frac{\partial \Phi_n}{\partial p} & \frac{\partial \Phi_n}{\partial h_1} & \cdots & \frac{\partial \Phi_n}{\partial h_N} & \frac{\partial \Phi_n}{\partial T_{\mathrm{t},1}} & \cdots & \frac{\partial \Phi_n}{\partial T_{\mathrm{t},N}} \end{bmatrix}. \tag{4.37}$$

It is worth noting that the system order n is related to the number of finite volumes N by

$$n = 2N + 1. \tag{4.38}$$

The Jacobian matrix Equation 4.37 can be given full rank by assigning the states $[p, h_1, \cdots, h_N]$ to $[\Phi_2(x), \Phi_3(x), \cdots, \Phi_{N+1}(x)]$, respectively, and by designating the remaining internal dynamics $[\Phi_{N+2}(x), \cdots, \Phi_n(x)]$ as any linearly independent combination of $N-1$ of the N individual tube temperatures. For simplicity, the first $N-1$ tube temperatures will be selected so that the internal dynamics, which will

now be referenced by the vector η, are represented by

$$\eta = \begin{bmatrix} p \\ h_1 \\ \vdots \\ h_N \\ T_{\mathrm{t},1} \\ \vdots \\ T_{\mathrm{t},N-1} \end{bmatrix}. \tag{4.39}$$

Due to the complexity of the system, a Lyapunov function proving the stability of the zero dynamics is difficult to find, so linearization will be used to analyze the local stability of various operating points. The linearization is carried out numerically where a constant $T_{\mathrm{a,in}}$, $\dot{m}_{\mathrm{a}}$, h_{in}, and $\dot{m}_{\mathrm{r,in}}$ are chosen. Since the presence of the zero dynamics requires that

$$y = \dot{y} = \cdots = y^{(r)} = 0, \tag{4.40}$$

the selected operating points are assumed to be steady state, and the operating points are found via Simulink. The assumption that the input and the disturbances are constant makes it possible to rewrite the system dynamics from Equation 4.2 as only a function of x:

$$\dot{x} = C(x), \tag{4.41}$$

and the linearization can be calculated based on [20] as

$$\dot{x} = A_{lin}x, \tag{4.42}$$

$$A_{lin} = \left.\frac{\partial C}{\partial x}\right|_{x=OP} = \left.\begin{bmatrix} \frac{\partial C_1}{\partial x_1} & \cdots & \frac{\partial C_1}{\partial x_n} \\ \vdots & \ddots & \vdots \\ \frac{\partial C_n}{\partial x_1} & \cdots & \frac{\partial C_n}{\partial x_n} \end{bmatrix}\right|_{x=OP}, \tag{4.43}$$

where A_{lin} is the Jacobian of Equation 4.41, and OP represents the steady state operating point. The Jacobian is calculated by using a forward-finite difference where a single state is increased by 0.01% and is then reset before the next state is increased. An example equation for the forward-finite difference for the first entry of Equation 4.43 is written as

$$\frac{\partial C_1}{\partial x_1} = \frac{C_1(1.0001x_1) - C_1(x_1)}{1.0001x_1 - x_1}. \tag{4.44}$$

If the eigenvalues of Equation 4.43 have real part less than zero, than the operating point is locally asymptotically stable [20]. This process is repeated for each combination of $T_{\mathrm{a,in}}$, $\dot{m}_{\mathrm{a}}$, h_{in}, and $\dot{m}_{\mathrm{r,in}}$, whose minimum and maximum values along with step sizes are displayed in Table 4.1.

Table 4.1: Disturbance and input values used in zero dynamics analysis.

Disturbance	Minimum	Maximum	Step Size
$T_{\mathrm{a,in}}$ [K]	298	314	2
$\dot{m}_{\mathrm{a}}$ [kg/s]	0.04	0.20	0.02
h_{in} [MJ/kg]	0.24	0.28	0.02
$\dot{m}_{\mathrm{in}}$ [kg/s]	0.01	0.08	0.005

Each set of eigenvalues calculated for each combination of values from Table 4.1 has all negative real parts, so the zero dynamics for the SMC can be concluded to be at least locally asymptotically stable.

The SMC is paired with the previously mentioned PI controller by selecting $\dot{m}_{\mathrm{out}}$ as the input, p as the output, and $\dot{m}_{\mathrm{in}}$ that is calculated from the SMC as a disturbance. The test bench, however, does not accept mass flow rates as inputs. In addition, the

individual tube temperatures as well as the individual air outlet temperatures are unavailable for measurement and thus for the controller, so the controller must be adapted in order to perform physical testing.

4.4 Controller Adaptation for Test Bench

Before testing on a physical system can occur, the controller must be modified to have inputs that are accepted by the test bench and to remove the need for individual tube and air outlet temperatures. The input $\dot{m}_{\text{in}}$ will be converted to the expansion valve opening using a model for the expansion valve, and $\dot{m}_{\text{out}}$ will be converted to the compressor speed with a model for the compressor. The tube and air outlet temperatures will be replaced with values that can be measured at the test bench using mathematical relations from subsection 4.3.1.

4.4.1 Expansion Valve

The expansion valve model from [23] is written as

$$\dot{m}_{\text{in}} = C_{\text{d}}(u_{\text{perc}})\sqrt{\rho_{\text{in}}\,(p_{\text{high}} - p_{\text{low}})}, \tag{4.45}$$

where $\dot{m}_{\text{in}}$ is the evaporator refrigerant inlet mass flow rate, C_d is the discharge coefficient, ρ_{in} is the density of the refrigerant entering the expansion valve, p_{high} is the refrigerant pressure on the high pressure side of the cycle, p_{low} is the refrigerant pressure on the low pressure side of the cycle, and u_{perc} is the percentage opening of the expansion valve and is considered the input. The valve model receives a desired mass flow rate from the SMC or the PID and the necessary refrigerant measurements, and Equation 4.45 is solved for u_{perc} to output the correct $\dot{m}_{\text{in}}$.

4.4.2 Compressor

The compressor model, also taken from [23], is expressed as

$$\dot{m}_{\text{out}} = \omega \cdot V_{\text{c}} \cdot \rho_{\text{in}} \cdot \eta_{\text{vol}}, \tag{4.46}$$

where $\dot{m}_{\text{out}}$ is the evaporator refrigerant outlet mass flow rate, V_{c} is the compressor volume, ρ_{in} is the density of the refrigerant entering the compressor, η_{vol} is the compressor volumetric efficiency, and ω is the compressor speed and is considered the input. Analogous to the expansion valve, the compressor model receives the desired outlet mass flow rate from the PI controller and the refrigerant density measurement, and the model is solved for ω.

4.4.3 Tube and Air Outlet Temperature Adjustments

Before the control law Equation 4.32 can be implemented, each $T_{\text{t},k}$ value and each $T_{\text{a,out},k}$ value, which comes from Equation 4.25, must be replaced with a value that can be measured. Since each $T_{\text{t},k}$ and $T_{\text{a,out},k}$ in the control law appear in the sum of all N volumes, equation Equation 4.27 can be used to write the sums of the N tube temperatures and the N air outlet temperatures as

$$\sum_{k=1}^{N} T_{\text{t},k} = \sum_{k=1}^{N} T_{\text{a,out},k} = N \cdot T_{\text{a,out}}. \tag{4.47}$$

Equation Equation 4.47 can then be substituted into Equation 4.32 to obtain the adjusted input

$$u_{\text{adj}} = -\frac{1}{b_{\text{adj}}} \left(h_{\text{adj}} + k \cdot \text{sat}(T_{\text{a,out}} - T_{\text{a,out,d}}) \right), \tag{4.48}$$

$$b_{\text{adj}} = \sum_{k=1}^{N} \left(\frac{b_{\text{r}} T_{\text{r},k}}{2 m_{\text{t}} c_{\text{t}}} \right) - \frac{b_{\text{r}} N \cdot T_{\text{a,out}}}{2 m_{\text{t}} c_{\text{t}}}, \tag{4.49}$$

$$h_{\text{adj}} = \sum_{k=1}^{N} \left(\frac{\left(a_{\text{r}} + b_{\text{r}} \frac{\dot{m}_{\text{out}}}{2}\right) T_{\text{r},k} + \dot{m}_{\text{a},k} c_{\text{p,a}} T_{\text{a,in}}}{m_{\text{t}} c_{\text{t}}} \right) - \frac{\left(a_{\text{r}} + b_{\text{r}} \frac{\dot{m}_{\text{out}}}{2} + \dot{m}_{\text{a},k} c_{\text{p,a}}\right) N \cdot T_{\text{a,out}}}{m_{\text{t}} c_{\text{t}}}. \tag{4.50}$$

Note that while $T_{\text{r},k}$ cannot be directly measured, it can be interpolated using the measured refrigerant pressure and the measured inlet and outlet specific enthalpies. The rest of the values in Equation 4.48 - Equation 4.50 can either be directly measured or are known parameters, so no observe is needed to use the controller. Before the SMC or PID controllers can be implemented on the test bench, they are simulated in Simulink in order to ensure safe operation and to obtain preliminary estimates of performance.

4.5 Controller Simulation

In order to prevent damage to the test bench, the controllers are simulated to ensure that various conditions are met. The temperature tracking must occur without extreme changes in the EXV opening or the compressor speed, and the refrigerant entering the compressor must be superheated in order to protect the compressor. Additionally, the refrigerant pressure must stay above a certain threshold, or else the test bench will shut down for safety reasons. To ensure the safety of the EXV and the compressor, limits to the rates of change of the EXV opening and to the compressor speed are imposed.

The desired air outlet temperatures during operation are first set between 2 °C and 12 °C, and a multitude of desired air temperatures within this range will be tested. To ensure robust performance of the controllers, the air mass flow rate $\dot{m}_{\text{a}}$, air inlet temperature $T_{\text{a,in}}$, and refrigerant inlet specific enthalpy h_{in}, which are considered the system disturbances, are randomized, and noise is added to the air mass flow rate. Noise could be added to the $T_{\text{a,in}}$ and h_{in} signals, but the effect on the system

performance is negligible, so noise-free signals are used for simplicity. Additionally, the high refrigerant pressure could be randomized, but its effect on the system is also negligible. The disturbance profiles used for each test are shown in Figure 4.3. The simulations will test the controllers in two separate trials. The first trial will involve steps of 1 °C from 12 °C down to 2 °C and back up. The second trial will involve steps between 2 and 5 °C from 12 °C down to 2 °C and back up for each step size.

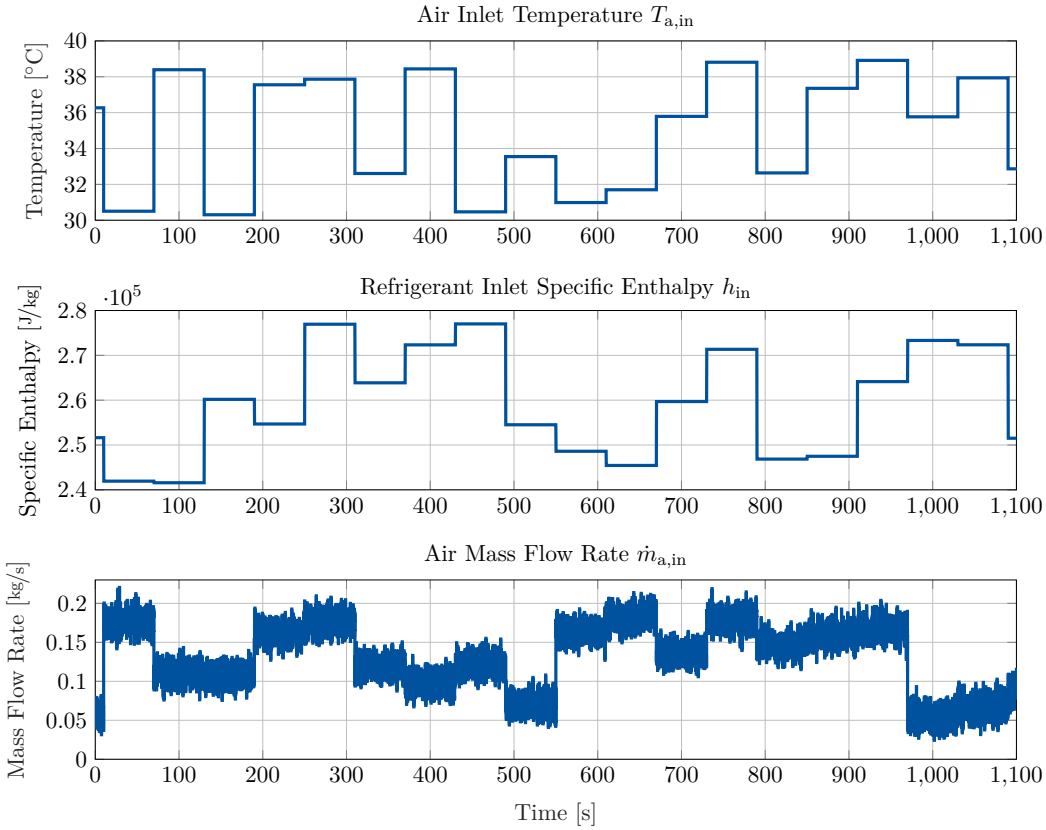

Figure 4.3: Profiles for each disturbance used in controller simulation.

The results of Trial 1 for the SMC are shown in Figure 4.4. Unfortunately, for the desired air temperature trajectory between approximately 310 and 450 s, the tracking cannot be achieved. This is explained by a system limitation related to the air mass flow rate, where as the air mass flow rate increases, the minimum achievable air outlet temperature also increases. Figure 4.5 visualizes this, where at an approximated maximum refrigerant mass flow rate rate, the minimum steady state air temperature

is plotted against the air mass flow rate for the lowest $T_{\mathrm{a,in}}$ and h_{in} and for the highest $T_{\mathrm{a,in}}$ and h_{in}. It must be noted that the maximum refrigerant mass flow rate may change depending on the high pressure side of the vapor compression circuit, so Figure 4.5 is meant to serve as an approximation.

In addition to the temperature tracking issues, the specific enthalpy of the refrigerant exiting the evaporator is not high enough for superheating, and the intermediate heat exchanger cannot be assumed to sufficiently increase the specific enthalpy. The issues present in this test occur in the other tests as well. Despite adjustments to both of the controllers, these problems could not be fixed, so an adjustment to the test itself is made.

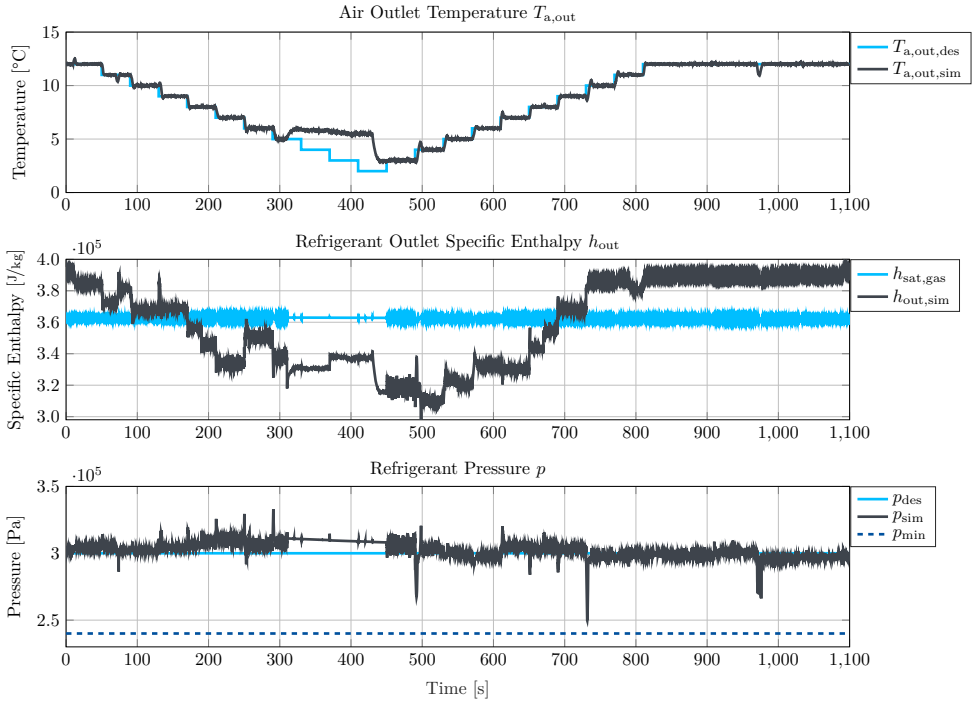

Figure 4.4: Results from SMC Trial 1 for desired temperatures between 2 and 12 °C.

The desired air temperatures are shifted to 10 to 20 °C with the same step sizes for each trial, and Figure 4.6 and Figure 4.7 show the temperature tracking results for Trial 1 and Trial 2, respectively, where it can be seen that both controllers are able to

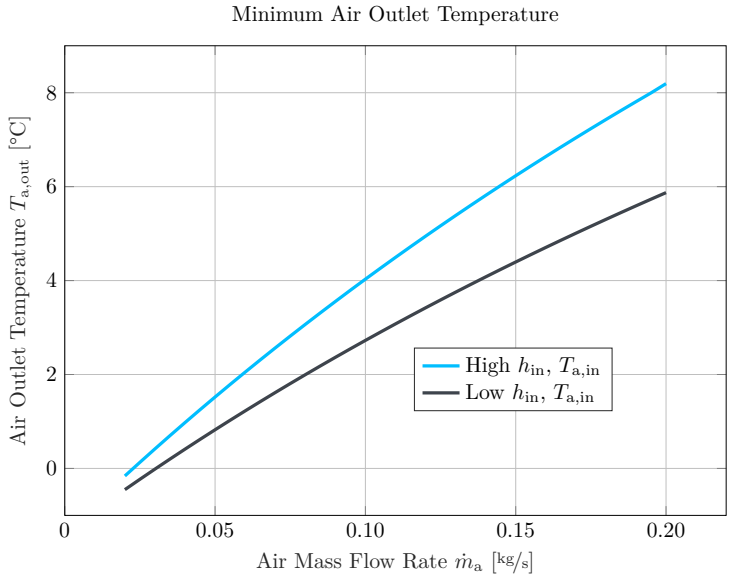

Figure 4.5: Minimum air outlet temperature vs. air mass flow rate.

track the desired temperature even in the presence of noise in the air mass flow rate signal. Jumps occur during a constant desired output temperature in Trial 1 at 190, 310, 550, 790, and 970 s. These jumps are more exaggerated for the PID controller, and they occur when the disturbances change, as can be confirmed with Figure 4.3. At 190, 310, and 790 s, the air inlet temperature change causes the air outlet temperature to change suddenly in the same direction. At 550 s, the air mass flow rate increases and causes the output temperature to increase. The largest jump occurs at 970 s, where both the air inlet temperature and the air mass flow rate decrease and cause the air outlet temperature to sharply decrease. Intuitively, these jumps make sense. When the air inlet temperature drops, less cooling is needed through the evaporator, and if the change is sudden, the system needs time to adjust. The same occurs for the air mass flow rate and agrees with what is observed in Figure 4.5. As the air mass flow rate decreases, the air in the evaporator takes longer to pass through and therefore has more exposure to the cooler evaporator structure. In a physical system, it can be assumed that the disturbances will not change as quickly as in the simulations, so

the frequency and size of the jumps in the output temperature will likely decrease.

Despite the jumps, both controllers are able to bring the air outlet temperature back to the desired value. The tracking performance of each controller is quantified by the mean temperature error (MTE), given as

$$MTE = \sum_{i=1}^{N_\mathrm{p}} \frac{\mid T_{\mathrm{a,out,sim}}(i) - T_{\mathrm{a,out,d}}(i) \mid}{T_{\mathrm{a,out,d}}(i)} \cdot \frac{1}{N_\mathrm{p}}, \tag{4.51}$$

where N_p, as in Equation 3.57, represents the number of data points in the set. Each MTE value is given in Table 4.2, and it can be seen that the SMC performance surpasses that of the PID. It is worth noting that the PID controller could be tuned to provide better temperature tracking, but it was found that this tuning causes the system to violate the safety requirements by either having the pressure or the outlet specific enthalpy go too low.

Table 4.2: Mean percent errors for each validation test.

	Trial 1	Trial 2
SMC	0.0566 °C	0.1814 °C
PID	0.1349 °C	0.2370 °C

The refrigerant pressure error is not quantified due to the fact that the necessary condition for the pressure is simply that it remains above the cutoff, which for the test bench used, is 2.4×10^5 Pa. Similar to the refrigerant pressure, the specific enthalpy of the refrigerant entering the compressor only needs to be above a certain threshold, which in this case is the saturated gas specific enthalpy. The specific enthalpies in Trial 2 dip slightly below the saturated gas value, but thanks to the intermediate heat exchanger, which is assumed to add 5 $^{\mathrm{kJ}}/_{\mathrm{kg}}$, the refrigerant exiting the evaporator can still be assumed to become superheated before entering the compressor. The pressure and specific enthalpy requirements are met for both trials of both controllers, and the profiles from both trials can be found in Figure 6.4 and Figure 6.5.

In a vapor compression refrigerant cycle, the compressor is the main work input

into the system [5]. Thus, investigation of the compressor speed for each trial provides further insight into the performance of each controller. The average compressor speeds for each trial, shown in Table 4.3, are used to make an initial comparison between the controllers. While the average speeds give a general idea of energy use, a more detailed model of the compressor power in relation to the compressor speed is required to confirm whether a certain controller uses less energy than the other. Thus, the results shown here serve only to provide a preliminary analysis.

Table 4.3: Mean compressor speeds for each validation test.

	Trial 1	Trial 2
SMC	27.8751 %	27.3773 %
PID	33.6523 %	32.0279 %

The average compressor speed in the SMC trials is noticeably lower than in the PID trials, and although this is only a rough comparison, this, along with the lower temperature errors shown in Table 4.2, demonstrates that the sliding mode controller may be more effective in a physical system than the PID controller.

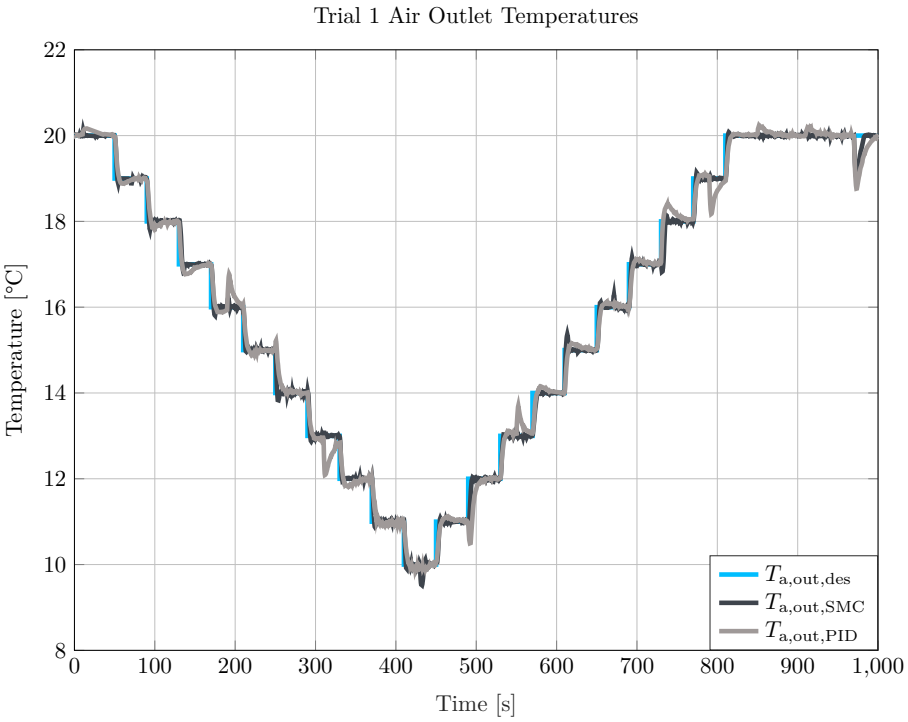

Figure 4.6: Trial 1 temperature tracking results.

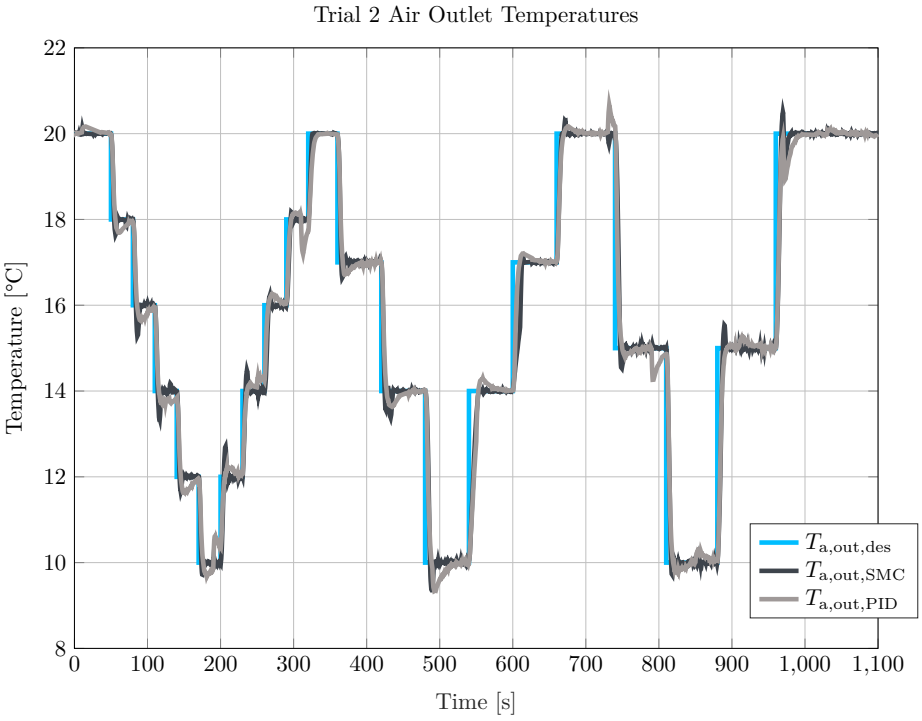

Figure 4.7: Trial 2 temperature tracking results.

CHAPTER 5
CONCLUSIONS AND FUTURE WORK

A model of the automotive evaporator used at the test bench was developed using first principles, and parameter identification was performed through minimization of a weighted error function with the refrigerant pressure, refrigerant outlet specific enthalpy, and air outlet temperature. The model performance was compared with several measured data sets, and the pressure tracking was excellent. Although the refrigerant specific enthalpy and air outlet temperature tracking could be improved, the model accuracy is sufficient for this application.

The controller simulation results presented in this work provide a proof of concept for use of a sliding mode controller in place of a PID controller. Unfortunately, the first set of desired temperatures could not be reliably reached, and the refrigerant specific enthalpy at the outlet was too low for safe operation. Shifting the desired temperatures up by 8 °C fixed both of these issues, and both controllers were also robust to signal noise and randomized disturbances. The SMC outperformed the PID in both temperature tracking and mean compressor effort and seemed less affected by the sudden changes in the disturbance values. While the simulations offer a reasonable idea of the performances of each controller, physical testing must be carried out in order to verify the results presented here. Based on the refrigerant pressure and specific enthalpy results, both controllers can be safely implemented at the test bench.

As with every project, further work can be done, such as improving the evaporator model, increasing the cooling ability of the system, and testing the controllers on the test bench and eventually within vehicles. The heat transfer coefficients for the air and the refrigerant were estimated as a linear function of their respective mass flow rates, but the evaporator manufacturer may be able to provide a more accurate function

as in [7]. Additionally, the refrigerant heat transfer coefficient was assumed to be identical for each phase, so estimating this coefficient separately for each phase and using more advanced functions as [7] may also provide more model accuracy. A more thorough model may also take humidity into account as in [13]. For now, however, the effects of humidity were assumed to be negligible.

One potential method to increase the cooling ability is to design a multi-input multi-output (MIMO) sliding mode controller that utilizes the inlet and outlet refrigerant mass flow rates as inputs and the air outlet temperature and refrigerant outlet specific enthalpy or the refrigerant pressure as outputs. The stability of this controller is demonstrated in [15]. If the MIMO SMC is designed with the method used in [15], an observer would also need to be designed. This stems from the requirement of knowledge of the value of each finite volume's refrigerant specific enthalpy in order to calculate the rate of change of the pressure or the outlet specific enthalpy. A MIMO SMC design was tested in simulation, but the inverted matrix, which is analogous to the inverted b term in the SISO SMC presented in Chapter chapter 4, was nearly singular and caused computational issues. Further investigation is needed to solve this issue, but for this work, focus was placed on the SISO SMC.

Since the controllers designed in Chapter chapter 4 satisfied the safety requirements, they are ready for implementation on the test bench. Testing on the bench before testing in a vehicle is crucial to be sure no important elements were missed within the simulations. The same temperature cycles used for the simulations can be used at the test bench, although the disturbance values will be different since they take up to a minute to change and do not do so instantaneously. The air mass flow rate and inlet temperature values can be selected at the bench, but the refrigerant inlet specific enthalpy depends on the other components in the system. After testing at the bench is complete and the system is shown to run safely, vehicle implementation and testing can begin. Contrary to the test bench, the air mass flow rate and

inlet temperature in the vehicle are uncontrollable, which is why these variables are treated as disturbances in the control design.

CHAPTER 6

APPENDIX

A.1 Model Validation Results

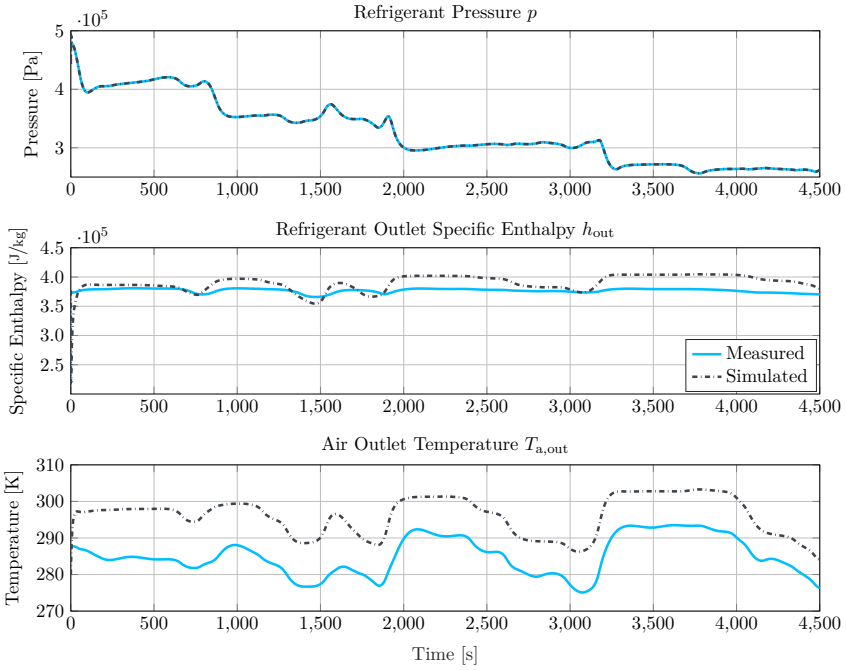

Figure 6.1: Results from validation 2.

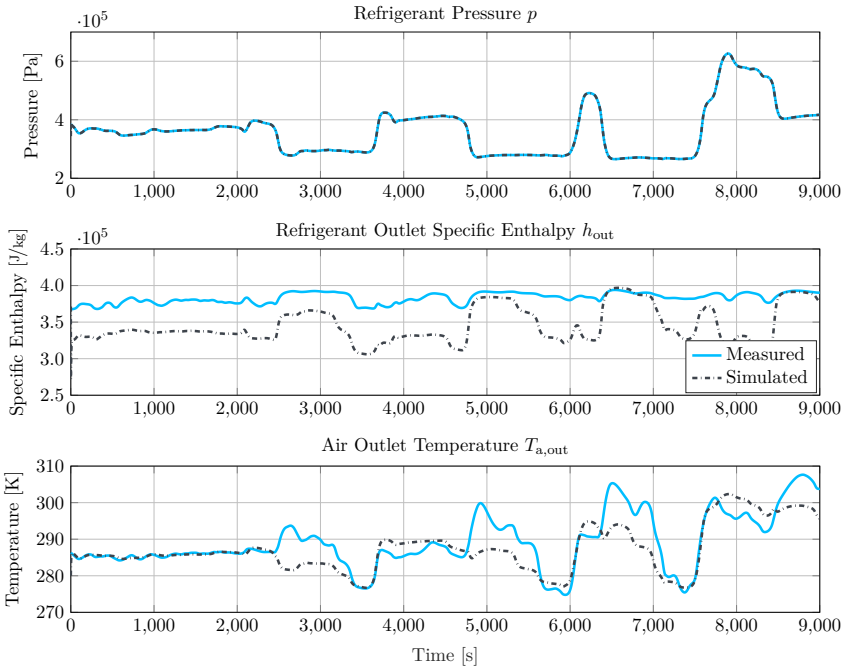

Figure 6.2: Results from validation 3.

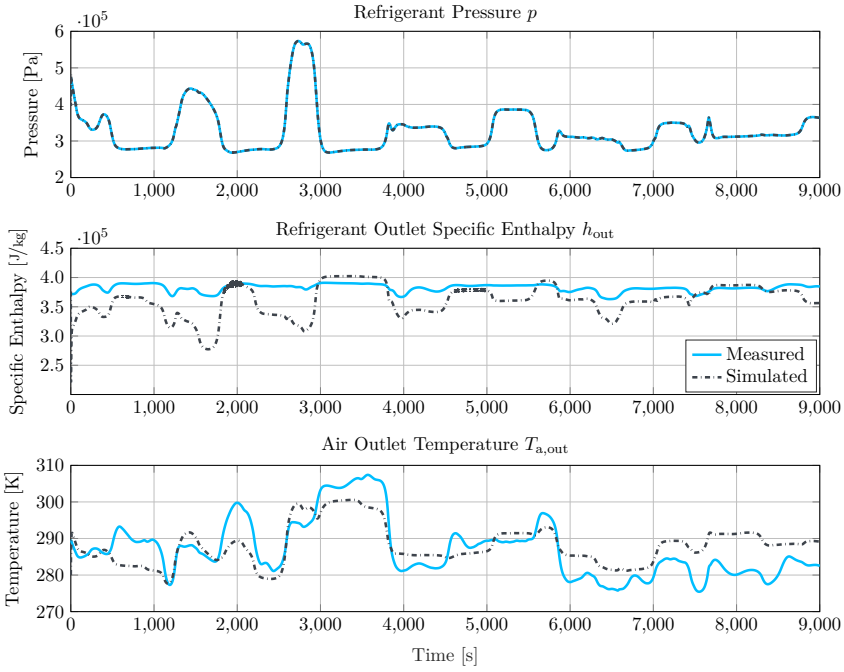

Figure 6.3: Results from validation 4.

A.2 Controller Simulation Pressure and Specific Enthalpy Results

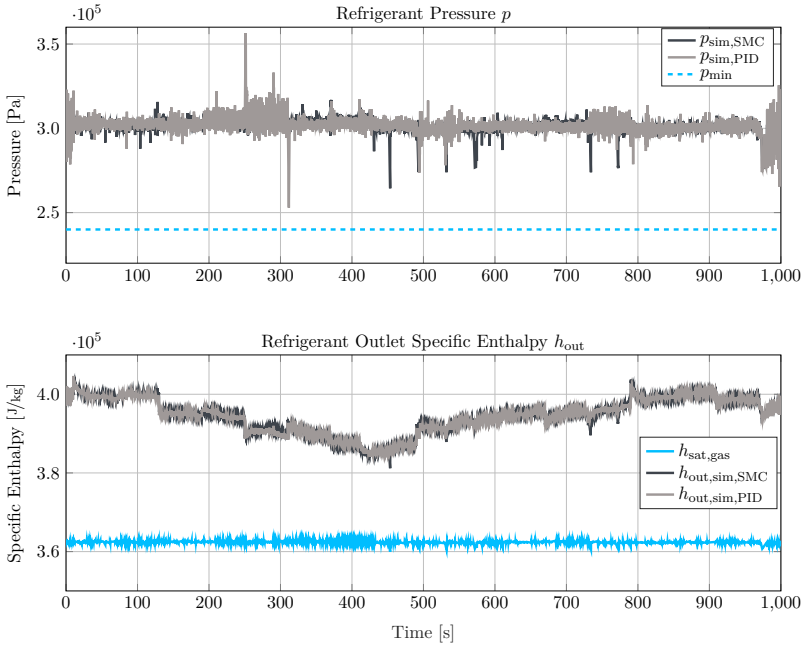

Figure 6.4: Pressure and specific enthalpy results for Trial 1.

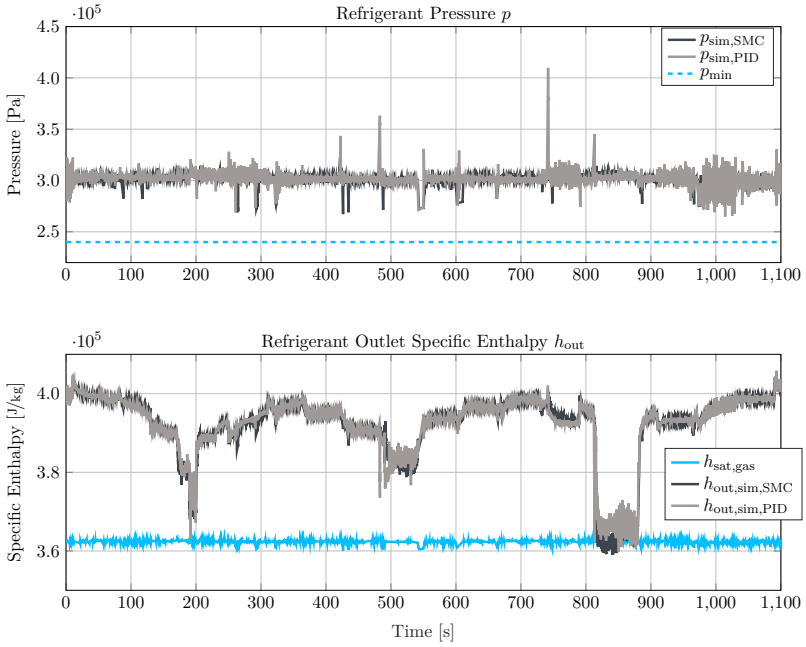

Figure 6.5: Pressure and specific enthalpy results for Trial 2.

REFERENCES

[1] R. K. Pachauri, Climate change 2014 : synthesis report. Geneva, Switzerland: Intergovernmental Panel on Climate Change, 2015, ISBN: 9789291691432.

[2] R Farrington and J Rugh, "Impact of vehicle air-conditioning on fuel economy, tailpipe emissions, and electric vehicle range: Preprint," Sep. 2000.

[3] Z. Zhang, C. Liu, X. Chen, C. Zhang, and J. Chen, "Annual energy consumption of electric vehicle air conditioning in china," Applied Thermal Engineering, vol. 125, pp. 567–574, Oct. 2017.

[4] M. B. Hmidene, "Dynamische modellierung eines kältekreislaufes mit fokus auf den kondensator," M.S. thesis, Institut für Systemdynamik, Universität Stuttgart, Mar. 25, 2020.

[5] M. Moran, Fundamentals of engineering thermodynamics. Hoboken, NJ: Wiley, 2014, ISBN: 9781118820445.

[6] Schulungshandbuch kälte-klima, Webasto, Dec. 2000.

[7] S. Bendapudi, J. E. Braun, and E. A. Groll, "A comparison of moving-boundary and finite-volume formulations for transients in centrifugal chillers," International Journal of Refrigeration, vol. 31, no. 8, pp. 1437–1452, Dec. 2008.

[8] T. L. McKinley and A. G. Alleyne, "An advanced nonlinear switched heat exchanger model for vapor compression cycles using the moving-boundary method," International Journal of Refrigeration, vol. 31, no. 7, pp. 1253–1264, Nov. 2008.

[9] D. Seitz, Modellbasierte Regelung eines Abgaswärmenutzungssystems für schwere Nutzfahrzeuge. Aachen: Shaker, 2019, ISBN: 9783844064650.

[10] T. L. Bergman, Fundamentals of heat and mass transfer. Hoboken, NJ: Wiley, 2011, ISBN: 9780470501979.

[11] R. Schwarze, CFD-Modellierung. Springer-Verlag GmbH, Oct. 19, 2012, ISBN: 9783642243783.

[12] D. Leducq, J. Guilpart, and G. Trystram, "Non-linear predictive control of a vapour compression cycle," International Journal of Refrigeration, vol. 29, no. 5, pp. 761–772, Aug. 2006.

[13] Y. Yao and Y. Yu, Modeling and Control in Air-conditioning Systems. Springer Berlin Heidelberg, 2017.

[14] G. Bejarano, J. A. Alfaya, D. Rodríguez, F. Morilla, and M. G. Ortega, "Benchmark for PID control of refrigeration systems based on vapour compression this work was supported by MCeI (grant DPI2015-70973-r).," IFAC-PapersOnLine, vol. 51, no. 4, pp. 497–502, 2018.

[15] A. Benamor, L. Chrifi-alaui, H. Messaoud, and M. Chaabane, "Sliding mode control, with integrator, for a class of mimo nonlinear systems," Engineering, vol. 03, no. 05, pp. 435–444, 2011.

[16] Y. Shtessel, C. Edwards, L. Fridman, and A. Levant, Sliding Mode Control and Observation. Springer New York, 2014.

[17] M. A. Johnson and M. H. Moradi, Eds., PID Control. Springer-Verlag, 2005.

[18] P. Skogestad, Multivariable Feedback Control. John Wiley & Sons, Oct. 26, 2005, 592 pp., ISBN: 047001167X.

[19] A. E. Choque-Rivero, "Hurwitz polynomials and orthogonal polynomials generated by routh–markov parameters," Mediterranean Journal of Mathematics, vol. 15, no. 2, Feb. 2018.

[20] H. Khalil, Nonlinear Systems: Pearson New International Edition. Pearson Education Limited, Nov. 1, 2013, 560 pp., ISBN: 1292039213.

[21] J.-J. E. S. W. Li, Applied nonlinear control. Englewood Cliffs, N.J: Prentice Hall, 1991, ISBN: 0130408905.

[22] A. Isidori, Nonlinear Control Systems. Springer London, 1995.

[23] A. G. Rasmussen Bryan P.; Alleyne, "Dynamic modeling and advanced control of air conditioning and refrigeration systems," Air Conditioning and Refrigeration Center. College of Engineering. University of Illinois at Urbana-Champaign., Tech. Rep., Jun. 2006.